Revision 2. Planar microstructures in zircon from paleo-seismic zones

Elizaveta Kovaleva[1,]*, Urs Klötzli[1], Gerlinde Habler[1] and John Wheeler[2]

[1] Department of Lithospheric Research, Faculty of Geosciences, Geography and Astronomy, University of Vienna, Althanstrasse 14, A-1090 Vienna, Austria

[2] Department of Earth, Ocean and Ecological Sciences, School of Environmental Sciences, University of Liverpool, L69 3GP, Liverpool, United Kingdom

* Corresponding author. E-mail: elizaveta.kovaleva@univie.ac.at

Abstract

Pseudotachylytes resulted from frictional melts associated with ultramylonites in high-grade metapelitic rocks from the Ivrea-Verbano zone in the Southern Alps (Northern Italy) were studied with focus on the deformation microstructures in zircon. The aims were to investigate the characteristics of zircon deformation in seismic zones, and to recognize specific microstructures generated in zircon during earthquakes, which could be useful for mineral dating of paleo-seismic events; helps to understand how seismic energy is released at depth and interacts with metamorphic processes.

The interior of polished zircon grains ranging from 30 to 150 μm in length were investigated with optical microscope and scanning electron microscope (SEM) techniques, including secondary electron (SE), backscattered electron (BSE), forward scattered electron (FSE), cathodoluminescence (CL) imaging, and crystallographic orientation mapping by electron backscatter diffraction analysis (EBSD). Grains were studied in situ and as separated fractions embedded in epoxy discs. Among different cataclastic and crystal-plastic deformation microstructures in zircon we identified characteristic planar deformation bands (PDBs), planar fractures (PFs) and curviplanar fractures (CFs).

Planar deformation bands in zircon are crystallographically controlled planar lattice volumes with misorientation from the host grain, which varies from 0.4□ to 2.7□. PDBs are usually parallel to {100} crystallographic planes, have width from 0.3 to 1 μm and average spacing of 5 μm in 2D sections. Planar deformation bands appear as contrast lamellae in orientation contrast images and in EBSD maps, and in rare cases can be observed with the optical microscope. PDBs form in specifically oriented grains due to high differential stresses, high temperatures and high strain rates generated in seismically active environment and/or due to shearing in the vicinity of frictional melts. Discovered structures represent a result of crystal-plastic deformation of zircon grains with operating dislocations having <100>{010} glide system and <001> misorientation axis, therefore, they can be classified as a new type (IV) lattice distortion pattern, according to the existing classification for zircon (Piazolo et al. 2012; Kovaleva et al. 2014).

We have demonstrated that formation of planar fractures in zircon takes place not only during impacts, but also in seismically active zones. We observe at least two cases of formation of PFs with {100} orientation: a) as a result of evolution of PDBs in association with PFs; b) as micro-cleavage.

This study demonstrates that planar microstructures in terrestrial zircon do not exclusively form during impact events, but also as a result of seismic events at depth due to unusually high differential stress, strain rate and temperature. According to the new findings, PDBs in zircon from the deep-crust are supposed to represent newly recognized evidence of seismicity.

Keywords: Electron Backscatter Diffraction (EBSD), zircon, shear zone, pseudotachylytes, planar deformation bands, planar fractures, crystal-plastic deformation

Introduction

Pseudotachylytes in mylonites

Pseudotachylytes are quenched frictional melts formed along fault planes due to coseismic sliding are described in many silicate rocks. Pseudotachylytes can convey information about depth, energy and mechanics of paleo-earthquakes (e.g. Pittarello et al. 2008). They are not only found in cataclastic rocks, but can also be associated with mylonites, pointing to deeper crustal levels of formation (Passchier 1982; Austrheim et al. 1996; Lund and Austrheim 2003; Austrheim and Corfu 2009; Pittarello et al. 2012). Mylonites represent zones of enhanced ductility within the lithosphere (Ranalli 1995); to nucleate and evolve, they generally require some structural heterogeneity (Pennacchioni and Mancktelow 2007). The mutual overprinting of pseudotachylytes and ultramylonites in metagabbro and felsic metapelites of Ivrea-Verbano zone (IVZ) was described in detail in Pittarello et al. (2012) who show that pseudotachylytes acted as precursor heterogeneities for strain localization and that ultramylonite formation immediately followed the post-seismic stress relaxation. Cycles of brittle/frictional and ductile/viscous shear zone formation could have repeatedly alternated.

So far the most reliable evidence of paleo-earthquakes was formation of pseudotachylytes (e.g. Sibson 1975; Austrheim et al. 1996; Pittarello et al. 2012). Planar and non-planar fractures and other microstructures have been previously described in garnet (Austrheim et al.1996) and zircon (Austrheim and Corfu 2009) and interpreted to be the evidences of seismic activity. More recently Angiboust et al. (2012), Austrheim (2013), Yang et al. (2014a, 2014b) have interpreted breccia and specific metamorphic structures in eclogites as seismically-induced. In our study we investigate zircons from ultramylonites associated with pseudotachylyte veins, and provide microstructural evidence of paleo-seismic activity recorded in zircons from the deep crustal section of the IVZ.

Planar microstructures in zircon

In the current context the term “planar microstructures” comprises all groups of different planar features described for zircon, including planar deformation features (PDFs), planar fractures (PFs), microcleavage, shock twins, phase transition along the certain planes and planar deformation bands (PDBs).

Planar deformation features (PDFs) in zircon, as defined by Erickson et al. (2013a), are shock-induced planar lamellae that crosscut the zircon crystal lattice along specific crystallographic planes and are filled with amorphous material or so-called “diaplectic glass”; or represent lattice domains with a high defect density (Leroux et al., 1999; Timms et al., 2012b; Grange et al. 2013). Planar lamellae filled with amorphous material have not been yet documented in natural terrestrial zircon samples (Erickson et al. 2013a) and the phenomena defined as PDFs in natural terrestrial zircon are usually planar fractures (e.g. Bohor et al. 1993; Corfu et al. 2003). But Timms et al. (2012b, fig. 8) and Grange et al. (2013, fig. 12) describe true PDFs in lunar zircon. These are identified by optical microscopy, in EBSD maps representing planes of low EBSD pattern quality, and in rare cases as dark lines in CL images. The crystallographically-controlled thin (<200 nm) layers of amorphous material or “diaplectic glass” were produced experimentally by Leroux et al. (1999). PDFs occupy {320} and {110} (Leroux et al., 1999) and also {112} and {001} (Timms et al. 2012b) crystallographic planes in zircon and result from 40 GPa shock pressure (Leroux et al. 1999), being considered to be indicative of shock pressure.

Planar fractures (PFs) or parallel and closely-spaced open structures resembling cleavage, are well-known from terrestrial and lunar impactites (e.g. Bohor et al. 1993; Kamo et al. 1996; Kalleson et al. 2009; Cavosie et al. 2010; Moser et al. 2011; Erickson et al. 2013a, 2013b; Thomson et al. 2014). These shock-produced fractures are particularly noticeable in minerals such as quartz, garnet, monazite and zircon, which do not normally reveal any cleavage in most terrestrial tectonic settings (Timms et al. 2012b). PFs in zircon are usually detected by scanning electron microscopy (SEM) on etched surfaces (e.g. Bohor et al. 1993; Kamo et al. 1996; Erickson et al. 2013a, 2013b; Thomson et al. 2014), and are often visible in the transmitted or reflected light microscope (Corfu et al. 2003; Thomson et al. 2014). Representing open structures, PFs can be filled with other material, and become noticeable in CL-images tracing as bright or dark patterns decorated by voids and pores. PFs can offset growth zonation (e.g. Kalleson et al. 2009; Cavosie et al. 2010; Moser et al. 2011; Erickson et al. 2013a, 2013b; Thomson et al. 2014); some PFs cause crystal lattice rotations from 1 to 10° (Erickson et al. 2013a). PFs in natural zircon are most frequently parallel to the {100}, {001}, {112} and {011} planes (Cavosie et al. 2010; Erickson et al. 2013a; Leroux et al. 1999). In experimental samples they also occupy (201), (211), (221) and (111) planes (Leroux et al. 1999).

Apart from planar fractures, sets of roughly parallel non-planar or curviplanar fractures (CFs) are also considered to be associated with impact events (Cavosie et al. 2010; Moser et al.

2011; Timms et al. 2012b; Erickson et al. 2013a). They may be crystallographycally-controlled and may act as channels for impact melt (Moser et al. 2011; Erickson et al. 2013a).

Shock twins or microtwins are considered to be a characteristic feature of shock-deformed zircon grains (Leroux et al. 1999; Moser et al. 2011; Timms et al. 2012b; Erickson et al. 2013a, 2013b; Thomson et al. 2014). They were documented with EBSD mapping and TEM imaging and occupy {110} crystallographic planes with twin individuals rotated at 65° to the host lattice.

Reidite, the high-pressure shock induced polymorph of zircon with scheelite structure was documented with TEM occurring along {100} planes. Shock twins and reidite formation indicate shock pressure above 40 GPa (Leroux et al. 1999).

Planar deformation bands (PDBs) in zircon were described as planar portions of crystal lattice parallel to {100} planes, with few to hundreds of micrometers thickness showing misorientation up to 10° with respect to the host grain (Nemchin et al. 2009, Fig. 1; Timms et al. 2012b, Fig. 5). PDBs form two orthogonal sets crosscutting the initial growth zoning. They can be revealed only by orientation- and EBSD mapping. The most common misorientation axes for PDBs are <001>, and the geometry of dislocation glide system, therefore, is considered to be <100>{010}. This is characteristic not only for impact-related dislocations (Leroux et al. 1999; Timms et al. 2012b), but also a dominant glide system in tectonically-deformed zircon grains (e.g. Reddy et al. 2007; Kaczmarek et al. 2011; Piazolo et al. 2012; Kovelava et al. 2014).

Otherwise oriented planar microstructures in zircon were produced during shock recovery experiments by Leroux et al. (1999). At shock pressure of 20 GPa planar fractures or micro-cleavage along {100} and sometimes {310} planes were formed. Multiple dislocations indicate that shock-related intense crystal-plastic deformation occurs. Sometimes shock-related dislocations are aligned in narrow "*micro-bands*", occupying glide planes {100}, which possibly could act as precursor for planar fractures.

However, shock-induced structures are not the only planar structures known in zircon. Some parallel parting has been observed in zircons from upper crustal xenoliths (Rudnick and Williams, 1987; Chen et al., 1994) and interpreted to form due to rapid decompression (Rudnick and Williams, 1987). Kresten et al. (1975) report on perfect partings or cleavages extending in several directions in kimberlitic zircon. Although such structures never appear to be perfectly parallel, as shock-induced structures do.

Motivation and challenge

After all, the classical definition of planar microstructures in zircon (especially for PDFs and PFs) exclusively ascribes their formation to shock metamorphism during impact events (Corfu et al. 2003; Timms et al. 2012b). However, planar microstructures in zircon that are not directly related to shock metamorphism were reported by Austrheim and Corfu (2009) in pseudotachylytes from the Svarthumlevatnet metagabbro, South-Central Norway. At few zircon grains presented in their study reveal sets of planar microstructures, which are visible in CL-images and considered to represent PDFs. These planar microstructures were assumed to have formed at very high strain rates during the formation of pseudotachylytes. Among other seismic-related deformation structures in zircon the authors also describe fragmentation of zircon and subparallel faults decorated by inclusions.

Our study also reveals planar microstructures in zircon which are formed during a deep crustal seismic event in association with pseudotachylytes. Under extraordinarily high differential stress, temperature and strain rate, zircon grains with favorable crystallographic orientation can develop crystallographically-controlled parallel lamellae, or planar deformation bands. These have not been previously described for terrestrial rocks, thus enhancing our knowledge on zircon rheology in an uncommon geological environment.

Geological and field settings

Samples were collected from the Ivrea-Verbano zone (IVZ) at Premosello in the Val d'Ossola (Northern Italy). Geological map of the area and sampling location is presented in Pittarello et al. (2012), Fig. 1. IVZ forms a NE-SW trending, steeply dipping sequence of meta-pelitic to -psammitic and meta-igneous basic rocks in the SE, ultrabasic mantle tectonites and a large underplated igneous complex in the NW. Peak metamorphic grade increases progressively from amphibolite facies in the SE to granulite facies in the NW. The IVZ is supposed to represent a section through the lower continental crust that experienced regional metamorphism during the uppermost Palaeozoic (Rutter et al. 2007; Quick et al. 2009), tectonically uplifted and delimited by the Insubric line from the NW and by the Pogallo line from the SE.

Within the IVZ a network of high-temperature shear zones oriented subparallel to the NE-SW elongation of the IVZ is observed. The shear zone network extends from Anzola (Val d'Ossola) to Forno (Val Strona) and can be traced for more than 20 km in length (Brodie et al. 1992). Single shear zones range in width from a few centimeters to more than 10 meters, and are rarely up to 200 meters thick. Mylonites in the northern part of the IVZ consist of interlayered metagabbro and depleted metapelites. Both rock formations completely (re-)equilibrated under granulite- and amphibolite-facies conditions during crustal attenuation/extension and contemporaneous magmatic underplating (Rutter et al. 2007) between 315 Ma and 270 Ma (Rutter et al. 2007; Quick et al. 2009; Sinigoi et al. 2011; Klötzli et al. 2014). In the Val d’Ossola section at Premosello peak *P*-*T* conditions are estimated at 0.6-1.0 GPa and > 800 °C, based on the data from neighboring Val Strona di Omegna (Redler et al. 2012).

Pseudotachylytes are found in mylonitic metagabbros and metapelites deformed under amphibolite to granulite facies metamorphism in the northern part of IVZ (Techmer et al. 1992; Pittarello et al. 2012). Pseudotachylytes are often overprinted by ultramylonites and interpreted to have formed coevally (Pittarello et al. 2012). The peak *P*-*T* estimates of pseudotachylyte formation yielded 550-650 □C and 0.4-0.6 GPa (Pittarello et al. 2012 and references therein).

Samples were taken from two outcrops at Premosello (N46°00'15.04"/E08°19'44.11" and N46°00'23.65"/E08°19'41.66"); each outcrop reveals several tens of meters thick layers of tectonically faulted, mylonitized and foliated felsic metasediments (Fig. 1a). At the hand specimen and thin section scale these mylonites contain dark shear zones that represent an association of ultramylonites and pseudotachylytes (Fig. 1b).

Analytical methods and data representation

Sample preparation

Zircon grains were examined in polished thin sections of rock chips and in grain separates embedded in epoxy resin. For the latter zircon grains were extracted from the host rock by the standard procedure involving rock crushing, sieving to the 300 μm size, density separation on a Wilfley table, in heavy liquids and with Frantz magnetic separator. All samples were mechanically polished with 0.25 μm diamond paste and subsequently chemically polished with alkaline colloidal silica solution on an active rotary head polishing machine for 4 hours. Samples were cleaned in ethanol and distilled water before carbon coating that was applied to establish electrical conductivity.

Scanning electron microscopy and cathodoluminescence (CL) imaging

All zircons were identified and characterized by backscattered-electron (BSE) and cathodoluminescence (CL) imaging in order to reveal the internal microstructures, using a FEI Inspect S scanning electron microscope equipped with a Gatan MonoCL system (Center of Earth Sciences, University of Vienna, Austria). Energy-dispersive X-ray spectrometry (EDS) was applied to identify the host phases. Imaging conditions were 10 kV accelerating voltage, CL-image resolution: 1500*1500 to 2500*2500 pixels using a dwell time of 80.0-150.0 ms and probe current/spot size 4.5-5.0.

Forward scattered electron (FSE) imaging and electron backscatter diffraction (EBSD) analysis

Zircon grains were examined for potential crystal-plastic deformation structures using orientation contrast images that were taken using a forescattered-electron detector (FSD) mounted on the EBSD-tube of a FEI Quanta 3D FEG instrument (Faculty of Geosciences, Geography and Astronomy at the University of Vienna, Austria). For FSE imaging the EBSD tube has been retracted by c. 5 mm in order to obtain maximum signal intensity on the FSD. After identification of the potentially deformed grains, EBSD orientation mapping was applied to selected zircon grains or grain domains. The FEI Quanta 3D FEG instrument is equipped with an EDAX Pegasus Apex 4 system consisting of a Digiview IV EBSD camera and an Apollo XV silicon drift detector for EDX analysis. EDX intensities and EBSD data were collected contemporaneously using the OIM data collection software v6.2.1. FSD settings and EBSD orientation mapping settings applied are discussed in details in Kovaleva et al. (2014). Orientation maps were obtained from beam scanning in hexagonal grid mode at step sizes of 0.1 – 0.2 micrometer.

Raw indexing for zircon grains is more than 99.99%. In some cases, after EBSD data collecting the maps were recalculated based on chemical composition of phases with the OIM v6.21 software.

All EBSD data are presented in the sample reference frames X-Z or Y-Z. The EBSD data are presented as EBSD pattern quality images, and as false color-coded misorientation maps, with colors showing the relative angular misorientation of each data point with respect to a user-selected single reference point within the grain. The reference point is indicated by a red marker in each EBSD map. The orientations of the crystallographic axes are plotted as lower hemisphere equal area projections and are color-coded according to the corresponding EBSD map. The EBSD maps and pole figures were produced using the EDAX OIM Analysis software v6.2.1. All FSE and EBSD maps as well as the pole figures are oriented with X (Y) positive up and Z positive left.

We also gained insight into geometrically necessary dislocation densities using Weighted Burgers Vector (WBV) calculations (Wheeler et al. 2009). Rectangular areas with WBV components were calculated over the EBSD maps with the MATLAB toolbox CrystalScape 1.3 based on the method described in Wheeler et al. (2009). For this goal the maps were transformed to a square grid and the Euler angles were recalculated accordingly with the Channel software. The actual algorithm used by Channel to import .ang files produces a square grid of data points and reduces the number of data points by approximately (√3)/2, which should involve some kind of interpolation to create the square grid. This may introduce errors – but the key point here is that in using the integral method to determine WBV, in which an integration path passes through many pixels, the effects of local errors are reduced and thus not compromise our interpretations. The rectangular areas, presented in this publication, are superimposed on the EBSD pattern quality maps with hexagonal grid, derived with EDAX OIM Analysis software, where deformation structures are better visible.

Petrography

Felsic mylonites represent strongly restitic, highly dehydrated metasedimentary rocks. They contain garnet clasts ranging from 50 to 500 μm in size (Fig. 1b), which are surrounded by a fine-grained foliated matrix consisting of alternating plagioclase- and quartz-rich layers, with intercalated biotite-ilmenite layers. Accessory minerals are zircon and monazite.

Locally pseudotachylytes are visible macroscopically as concordant dark-gray 2-3 mm thick veins, fractured and offset by fractures. More often they are hosted by ultramylonites from which they are hard to distinguish. Ultramylonitic shear zones in the felsic mylonites appear as 1-2 cm thick dark rock portions extending parallel to the main foliation and limited by subvertical fractures (Fig. 1b). Shear zones contain pseudotachylyte veins concordant with the foliation, intensively folded and offset by fractures (Figs. 1b; 2a-b; 2f-g).

Both pseudotachylytes and ultramylonites mainly represent an ultra-fine-grained matrix composed of plagioclase, quartz, biotite and ilmenite, with minor amounts of garnet. Unlike the mylonitic portions of the rock, the ultramylonite contains much less garnet clasts, and does not reveal monomineralic bands. The foliation in ultramylonite is represented by variations in the biotite-content. Pseudotachylytes can be occasionally distinguished from surrounding ultramylonites in optical microscope as homogeneously black layers in plane-polarized light (Fig.

2a), but more often as layers with bright rims in reflected light (Fig. 2f) and BSE images (Figs. 2b-c, 2g).

Pseudotachylytes are often rimmed by single garnets and garnet aggregates of second generation (Fig. 2), which is different from host rock garnets. These garnet grains have a dendritic morphology, range from 5 to 40 μm in size, and contain multiple inclusions, mostly ilmenite (Fig. 2d) as described by Austrheim et al. (1996), Austrheim and Corfu (2009) and Pittarello et al. (2012). Garnets rimming pseudotachylyte are supposed to form due to late low-temperature (about 550□) crystallization of garnet from the melt (Pittarello et al. 2012). Sometimes angular garnet fragments with dendritic overgrowths rim the injection veins. Such fragments form due to cataclasis of garnet porphyroclasts, dragging by melt and subsequent overgrowth by new dendritic rims (Pittarello et al. 2012).

Another feature characteristic for the pseudotachylytes are needle-shaped fine grains, ranging from 1 to 5 μm in length. Possibly these grains are locally preserved microlites, resulting from non-equilibrium crystallization of frictional melt (Figs. 2d and 2e).

In the sampled felsic mylonites, a fraction of 23-29% of all zircon grains are brittlely deformed, whereas 10-11% of all zircon grains show crystal-plastic deformation. These values are close to those for non-foliated metapelites sampled in the same area yielding about 24% brittlely and 11% crystal-plastically deformed grains, respectively. The content of deformed zircon grains in pseudotachylytes and in associated ultramylonites is much higher. There, 63-72% of grains are brittlely deformed (Fig. 3) and 19-28% show crystal-plastic deformation (Fig. 4), including grains with planar deformation bands (Figs. 5-8).

Microstructural and crystallographic zircon data

Planar deformation bands

Planar deformation bands (PDBs) represent slightly misoriented (0.4°-2.7°) planar grain portions crosscutting the zircon grains. PDBs in 2D sections trace in one or two directions and their amount varies from 2 (Fig. 5a) to several tens per grain (Fig. 6a) in each direction. The width of lamella traces in 2D sections varies from 0.3 to 1 μm, whereas at mutual intersections they show characteristic thickening (Figs. 5c and 5g, dashed circles). Misorientation from the host crystal may also slightly increase at the sites of mutual PDBs intersection. Spacing between PDBs ranges from 1 μm (Fig. 5a) to 25 μm, but most frequently is around 5 μm (Figs. 5e and 5i). These structures are oriented parallel to the {100} plane (Figs. 5d, 5h, 5l and 6c). In one case they trace parallel to the {001} (Fig. 6i).

PDBs can be identified in orientation contrast (FSE) images and EBSD pattern quality maps as dark or bright planar grain portions; in color-coded EBSD orientation deviation maps as lattice portions slightly misoriented with respect to the host. They are not visible in CL-images (Figs. 5-8) and some of the PDB sets are not visible in EBSD maps as well (Fig. 5g, NE-SW set; K, NE-SW set). Sometimes PDBs can be identified in the optical microscope as parallel lamellae (Fig. 6b, white arrows). Some PDB show steep misorientation profiles (e.g. Figs. 6d, 6h and 9), whereas some show blurred boundaries (Figs. 5c, 5k, 7c and 7f). In one case asymmetric PDBs are shown (Fig. 5g), which demonstrate abrupt misorientation change at left side and gradual orientation change towards the host grain orientation at the right side.

The true misorientation of the PDBs can be observed with misorientation profiles (Fig. 9) that are giving point-to-point and point-to-origin misorientation angles. The misorientation peaks clearly rise above the noise level, which usually does not exceed 0.3□. Peaks formed by point-to-origin misorientations (black line in Fig. 9) usually count one prominent peak for each PDB. They are a few µm thick and have an asymmetric shape, with one steeper and one shallower slope (Fig. 9a: intersection 1, 2, 3a, 4; B: intersection 1, 3; C: intersection 1). In some cases maxima can form a plateau (Fig. 9c, int. 1: 1 µm-wide plateau, int. 2: 0.5 µm-wide plateau).

The documented intragranular distortion indicates the presence of geometrically necessary dislocations in the lattice. For a selected sample region in the EBSD map, the Weighted Burgers Vector (WBV) quantifies the total Burgers vector for all the dislocations passing through that region (the “integral form” according to Wheeler et al. 2009). This can be expressed in terms of lattice vectors and then divided by the sample region area to measure dislocation density including Burgers vector direction. Using rectangular sample regions, the WBV calculation has shown that in the domains of crystal lattice where PDBs are not observed the WBV is comparatively low (Fig. 10, rectangle areas with gray lines). In domains where two sets of PDBs intersect, the WBV is large and shows mixed directions (Fig. 10, rectangle areas with thin black lines). In domains, intersecting one set of PDBs, WBV usually has a large *b* component (dashed lines), whereas in rare cases the *c* component (Figs. 10a and 10d, white lines) and for grain 46 the *a* component is large (Fig. 10c, dotted lines).

PDBs can be pinned by structures causing misorientation of grain fragments (grain 46, Figs. 5i-k, black arrow) and by preexisting open fractures with offsets (grains 17, 03b; Fig. 6). However, structures that do not generate misorientations or offsets do not influence the geometry of PDBs (Figs. 5i-j, white arrow; Fig. 6a). For example, in grain 17 (Figs. 6a-e) a set of subvertical fractures crosscut the zircon grain at the left and at the right generating offsets. PDBs do not crosscut these fractures but terminate at the boundary of the central fragment. On the other hand, the subhorizontal fracture, which is decorated by pores and displaced by the crosscutting subvertical fracture at the right hand side, does not influence the geometry of the crosscutting PDBs.

Occasionally, PDBs occur together with other crystal-plastic and brittle deformation structures. Grain 14 (Fig. 7a-c) shows lattice distortion by crystal-plastic deformation, it is crosscut by multiple fractures and contains PDBs which mainly appear in the EBSD orientation deviation map (Fig. 7c), crosscut the central part of the grain and intersect crystal-plastically deformed zones. PDBs seem to be slightly offset by a fracture (Fig. 7c, red dashed line). Grain 45 (Figs. 7d-f) also shows associated PDBs, fractures and lattice distortion (Fig. 7d, indicated by red arrow). PDBs cut across the fracture, but they seem to disappear in domains with lattice distortion (Figs. 7d and 7f, lower left).

Concerning the spatial distribution of the zircon grains revealing PDBs, these are observed at the contact between mylonites and ultramylonites, or in matrix within 1 cm from ultramylonites in 2D sections (Fig. 1b). Zircon grains hosted by central part of ultramylonites contain very indistinct PDBs that appear to be annealed. Approximately 3% of the separated large 100-300 μm crystals exhibit PDBs (e.g. grain 91, Figs. 8e and 8F).

Planar fractures

Planar fractures (PFs) occur less frequently than PDBs. Usually there are a maximum of 3-5 in one grain (Figs. 5e and 6a-b, black arrows; 8a and 8d, black arrows; 8e and 8f white arrows). They appear in BSE, SE and orientation contrast images as dark, straight, sometimes segmented lines (Figs. 5e, 6a, 8a and 8e). In rare cases, when PFs are thick enough and/or oriented normal to the thin section surface, can they be observed with transmitted light microscopy and in CL images as dark lamellae (Figs. 6b, 8b, 8d and 8f).

Sometimes PFs overprint PDBs (Figs. 5e, 6a and 8e) and in that case their trace consists of discontinuous fracture segments. However, they are not necessarily associated with PDBs (grain 21, Fig. 8a, black arrows), but in both cases they are oriented parallel to the {100} planes and therefore are crystallographically controlled.

In grain 43 one PF is fragmented along the PDB and the fracture tips form a double-wing shape (Fig. 5e, inset). Wings initiate at the sites of intersection with the orthogonal set of PDBs.

Curviplanar fractures

Two sets of CFs are visible in FSE and CL images of grain 26 (Figs. 4c and 4d). A set of subparallel CFs crosscut the overgrowth rim (trace orientation indicated by white arrows); they are open and oriented roughly parallel to a {100} crystallographic plane. These CFs are terminated by another fracture set.

In this grain we also observe subparallel trails of pores, in CL image these traces appear as bright lines, therefore these inclusion trails are interpreted as healed CFs. (Figs. 4c and 4d, black arrows). They only crosscut the magmatic core and do not continue into the overgrowth.

Grain 03b (Fig. 6f) is fractured by two subvertical CFs that prevent PDBs penetration into the left fragment of the grain.

In grain 21 two CFs (Fig. 8a, white arrows) are terminated by a planar fracture (Fig. 8a, intersection sites are highlighted by gray arrows). CFs in this case have a crystallographic orientation roughly parallel to a {110} plane.

Cataclastic deformation structures in zircon

Cataclastic deformation of zircon is abundant in the pseudotachylyte-bearing rock (up to 72%). Some of the grains are strongly fragmented (Fig. 3), which does not occur in mylonites and non-foliated metamorphic rocks of the study area. The fragmented zircon grains occur in the vicinity of pseudotachylytes, within fractures that crosscut and offset pseudotachylytes and ultramylonites at a high angle (Fig. 1b).

Grain 12 is crosscut by several transgranular fractures with displacement of the fragments (Fig. 3a, subhorizontal fracture trace); the magnitude of the offset in the thin section plane is particularly well visible in the CL image revealing the initial growth zoning, yielding 50 µm apparent sinistral offset in Figure 3b. Fragments of grain 12 also preserve crystal-plastic deformation structures, visible in orientation contrast (fig. 3a). Grain 04a is crosscut by one transgranular fracture (Fig. 3c, vertical), and fragmented by multiple sets of intragranular fractures. Grain 10 is embedded within an 80 µm-thick fracture zone and is strongly fragmented together with the surrounding phases (plagioclase, amphibole) (Figs. 3d and 3e). The fragments of zircon grain 10 and surrounding phases are mixed; they have similar size range and typical angular shapes. A set of open fractures crosscuts grain 26 (Fig. 4) but does not display significant offsets and neither causes rotation of the fragments. A fracture in grain 46 (Figs. 5i and 5k) cuts through PDBs and produces misorientation of the crystal lattice of about 1° (Fig. 5k). Fractures that have different chronological relationship with PDBs are also observed in grains 17 and 03b (Fig. 6), 14 and 45 (Fig. 7).

Crystal-plastic deformation structures

In rocks containing pseudotachylytes plastic deformation of zircon is reflected by gradual bending of the lattice, systematic rotation of crystallographic axes and formation of low-angle boundaries. Plastic deformation is also often associated with cataclastic deformation at the grain margins.

Grain 26 shows local lattice distortion in two domains (Fig. 4a). Domain i) belongs to a magmatic core that shows localized fragmentation at the left margin (Fig. 4d). The maximum misorientation of the lattice in domain i) is more than 20° with respect to a reference point in the undeformed part of the grain. The distorted edge shows bending from 1.5° to 10° per µm and the formation of low- and high-angle boundaries (with a threshold of 10°, as in Piazolo et al., 2012) with radial semi-circular shapes. In Fig. 4b low-angle boundaries of the domain i) are highlighted with red and green lines; grain boundaries with misorientation of more than 15° are highlighted with blue lines. Fragments are detached from the parent grain and become involved in the fine-grained matrix (Figs. 4a, 4c and 4d). This lattice distortion pattern corresponds to type (II) according to the classification for zircon given by Piazolo et al. (2012) and Kovaleva et al. (2014).

Domain ii) of grain 26 belongs to the overgrowth rim (Figs. 4a and 4d). The maximum misorientation in this domain reaches 15° and documents gradual bending at about 1° per µm around a rotation axis parallel to the [001] zircon direction (Fig. 4a, inset, in red circle) without low-angle boundary formation. This finite deformation pattern reveals the features of zircon lattice distortion type (I) (Piazolo et al. 2012; Kovaleva et al. 2014).

Grain 46 (Figs. 5i-l) reveals a low-angle boundary (Figs. 5j-l, black arrow) associated with a CL-bright 5 µm-thick band (Fig. 5j, white arrow). The CL-bright band associated with low-angle boundary could be a result of hydrothermal alteration, facilitated by lattice distortion (Fig.

5j). The low-angle boundary appears as dark linear feature in the EBSD pattern quality map (Fig. 10c, top), and as a step in orientation of about 1° in the EBSD orientation deviation map (Fig. 5k, indicated by black arrow). The low-angle boundary traces approximately parallel to the {001} plane (Fig. 5l). Grain 46 contains strain-free subgrains that are separated by low-angle boundary (highlighted by black arrow), and thus has the characteristic type (III) zircon lattice distortion pattern (Piazolo et al. 2012; Kovaleva et al. 2014). The WBV of subareas across this boundary shows large *a* component and sometimes a large *c* component (Fig. 10c), indicating that dislocation lines with Burgers vectors [100] and [001] are dominant (MacDonald et al. 2013). The PDBs present in the grain crosscut the CL-bright band but terminate at low-angle boundary.

Crystal-plastic deformation overprinting PDBs occur in grains 14 and 45 (Fig. 7). Grain 14 shows grain internal lattice rotation of more than 20° with respect to a reference point and represents lattice distortion pattern type (I) (Piazolo et al. 2012; Kovaleva et al. 2014), which is offset by a set of subhorizontal fractures as apparent in orientation contrast image (Fig. 7a). Grain 45 is deformed locally at its margin (Fig. 7d, red arrow); PDBs become indistinct where crystal-plastic deformation takes place.

Discussion

Characterization of planar deformation bands

Properties of PDBs. PDBs yield high-quality EBSD patterns and therefore cannot be considered as open structures or amorphous material. Furthermore they cannot be regarded as domains with high dislocation density like "micro-bands" (Leroux et al. 1999) or domains with damaged crystal lattice, including, for example, metamicted zones or damaged during sample preparation. If so, EBSD quality maps should consistently reveal them as dark domains, but, contrastingly, many PDBs are bright (Fig. 10). Based on these observations we conclude that PDBs are crystalline portions of the zircon lattice. PDBs cannot be traced in CL-images, which is not only consistent with low defect density (Reddy et al. 2006), but also indicates the lack of variations in CL-active trace elements (Reddy et al. 2006; Timms et al. 2006; Timms and Reddy 2009). Misorientation profiles reveal PDBs as tabular misoriented domains of up to 2.7° from the host grain orientation (Fig. 9).

Another characteristic property of PDBs is their ability to cut through healed fractures, if adjacent crystal fragments have not changed their mutual orientation. When the fracture is open (grains 17, 03b), PDBs do not crosscut, but terminate at the fracture. Any other boundary, which causes relative rotation of the crystal lattice, represents a limit for the extent of PDBs (e.g. grain 46 with low-angle boundary). We conclude that PDBs in zircons are strictly crystallographically controlled structures and any pre-existing significant lattice distortion can stop their propagation.

Dislocations and slip associated with PDBs. PDBs are likely separated from the host lattice by low-angle boundaries that are associated with dislocations, indicated by high WBV values for the lattice portions that contain PDBs (Fig. 10). Most of the WBV measurements across PDBs show the large *b* (grains 34, 43, 03a) or large *a* (grain 46) component of the WBV, that are relevant for tetragonal symmetry and could imply high amount of dislocation lines with Burgers vector <100> (Wheeler et al. 2009; MacDonald et al. 2013). <100> is the energetically preferable orientation of the Burgers vector as the shortest translation vector in the zircon structure (Leroux et al. 1999). Together with the geometry of PDBs that are parallel to {100} planes, this leads to a conclusion that the operating glide systems are <100>{010} with misorientation axis parallel to [001]. Those are the most frequently documented glide systems in naturally deformed zircon samples from different tectonic settings (e.g. Reddy et al. 2007; Kaczmarek et al. 2011; Piazolo et al. 2012; Timms et al. 2012a, 2012b; Kovaleva et al. 2014).

Preferred orientation of Burger's vectors that increase towards the PDBs shows that PDBs contain deformation-related rather than growth-related dislocations. Considering deformation-related dislocations associated with PDBs, these are supposed to be a result of crystal-plastic deformation. Although similar features have been described previously (Timms et al. 2012b; Grange et al. 2013), they do not fit into the existing microstructural classification scheme of Piazolo et al. (2012) and Kovaleva et al. (2014). Therefore, a new lattice distortion pattern classification, type (IV), is suggested for PDBs.

The glide directions <100> are activated under high differential stresses or ultrahigh shock pressure conditions (in case of impact-related microstructures) and at favorable orientation of the zircon lattice with respect to the local stress field. Indeed, there seems to be a specific orientation of zircon c-axes relative to the differential stress or shock wave that facilitates formation of c-axis parallel microstructures (Kaczmarek et al. 2011; Erickson et al. 2013a; Kovaleva et al. 2014).

Orientation of zircon crystals with PDBs. In Figure 11b we plotted crystallographic orientations of zircon grains with planar microstructures from the thin section shown in Figure 1b. Deformed grains show a strong [001] alignment parallel to X axis of the shear flow, whereas <100> show no systematic orientation to the kinematic reference frame. Even though the orientation of grains may have changed during the subsequent tectonic evolution of the rock, the clustering of the c-axes is still rather strong: 6 of 8 grains have c-axes oriented approximately parallel to the stretching lineation. Such a non-random distribution indicates that specific crystallographic orientation of grains in the sample is preferable for the formation of planar microstructures. This observation is not consistent with the theoretical model of crystal-plastic deformation in zircon by Kaczmarek et al. (2011), who suggested that zircons with c-axis parallel to the kinematic X form misorientation axes parallel to [100]. As we have shown above, dislocations associated with PDBs have misorientation axes [001].

Comparison of PDBs with PDFs. The structures that are described here as "planar deformation bands" or PDBs have strong similarity to so-called "planar deformation features" or PDFs that are well-known from zircon from impactites. Both types of structures are described as strictly parallel, crystallographically controlled portions of crystal lattice, with the visible width up to few micrometers and mean spacing of approximately 5-10 µm (Bohor et al. 1993; Corfu et al. 2003; Leroux et al. 1999; Erickson et al. 2013a; Timms et al. 2012b; Grange et al. 2013).

However, PDBs have principal differences from PDFs. PDFs described from impact-related zircon usually occupy the {001}, {110}, {112} and {320} crystallographic planes, and there are no reports of PDFs occupying {100} (Leroux et al. 1999; Timms et al. 2012b). Moreover, PDFs by definition should represent lamellae of amorphous material (Leroux et al. 1999; Erickson et al. 2013a). Therefore, PDFs are supposed to appear in CL images and show low EBSD pattern contrast. Unlike PDFs, PDBs described here do not appear in CL images and represent crystalline portions of the zircon lattice, because their EBSD quality pattern does not decrease relative to the host grain.

In addition, PDFs are often associated with shock twins (Leroux et al. 1999; Moser et al. 2011; Timms et al. 2012b; Erickson et al. 2013a, 2013b; Thomson et al. 2014) that form along the PDF planes. In our samples zircon twinning has not been observed.

PDBs presented here are similar to "planar deformation bands" described by Timms et al. (2012b) and Nemchin et al. (2009) and "planar features" described in Grange et al. (2013) in lunar zircon that was affected by shock metamorphism with partial metamictization ("oldest" zircon grain described multiple times in: Nemchin et al. 2009, Fig. 1; Timms et al. 2012b, Fig. 5; Grange et al. 2013, Figs. 10b, 12?). Those PDBs neither appear in BSE nor in CL images, but are clearly observed in the EBSD maps as planar portions with misorientation up to 10□. The misorientation profile looks similar to what is observed for PDBs presented here (Fig. 9). PDBs do not form a different phase and extend in two directions parallel to the {100} zircon planes (Timms et al. 2012b). Despite of the different formation environment and conditions, the PDBs reported by Timms et al. (2012b) and Grange et al. (2013) show strong similarities to the terrestrial PDBs described in our study.

Possible formation mechanisms of PDBs. The formation of PDBs in zircons from ultramylonites associated with pseudotachylytes can be explained as a result of:

a) Shock deformation, similar to deformation due to impact events;

b) High differential stress and strain rate during a compression stage of seismic wave propagation;

c) High differential stress and strain rate during tectonic shearing.

Even though PDBs resemble shock-induced deformation structures like PDFs and PFs, they were formed under completely different environmental settings. Contrasting with ultrahigh shock pressure generated at the Earth's surface during an impact event, earthquakes at depth generate significantly different stress fields and magnitudes. More specifically, peak pressure for seismic events in IVZ was estimated at 550 MPa (Khazanehdari et al. 2000). And, for example, transformation of quartz to coesite, which often happens during impacts, at a given temperature of 550□ C would require pressure of about 2,7 GPa (Akaogi and Navrotsky, 1984). To compare, estimations for pressure generated by meteorite impacting the earth surface could vary from 100 to 4000 GPa (Öpik, 1958). Although ultrahigh pressure mineral associations have been previously reported to be coeval for earthquakes (Yang et al. 2014a), but shock metamorphism have been not. On the other hand, deformation caused by an earthquake occurs in depth under lithostatic pressure, which may compensate shock pressure; lithostatic pressure is generally absent during impact-related shock deformation. We assume that scenario a) is unlikable for the PDBs formation.

Scenario b) is suggested in number of earlier studies: Leroux et al. (1999) do not explain the formation of micro-cleavage in 20-GPa experiment by shock waves, but rather due to shear stress during the compression stage. Consistently, Erickson et al. (2013a) reported initial development of {100} PFs in shocked zircon grains relative to other shock structures. This is explained by their formation during the shock loading stage (Erickson et al. 2013a), presumably induced by shear stress. Austrheim and Corfu (2009) explain formation of planar microstructures in zircon from pseudotachylytes by very high strain rates. Yang et al. (2014a) explain the formation of ultra-high pressure mineral assemblages in the dykes as a result of high stresses and friction-induced high temperatures that were coeval with the earthquake.

We suggest that high shear stresses and strain rates are responsible for PDBs formation in the studied sample material. Shear stresses, estimated by earthquakes can vary from 7 to 17 MPa at the depth of 2-10 km (estimation by Spudich et al. 1998). Even though impact shock pressure magnitudes are unlikely to be reached during seismic event, high strain rates are possible. This is indicated by intensively fragmented zircon grains in mylonites, broken and cleaved garnets in the host rock (Austrheim et al. 1996) and by presence of pseudotachylytes (Pittarello et al. 2008, 2012). Thus, newly found PDBs in zircon from the deep crust represent another evidence of paleo-seismicity.

Scenario c) suggests that the formation of PDBs is not directly related with the propagation of seismic waves, but with subsequent ductile shear zone formation accompanied by high stresses, strain rates and friction-induced high temperatures. This scenario is supported by the selective deformation of grains, which <c> are parallel to kinematic X (Fig. 11b). Thus, PDBs in those grains and associated low-angle boundaries are also parallel to kinematic X. Usually, geometric control of macroscopic kinematic frame on deformation microstructures imply their genetic relationship (Reddy and Buchan 2005; Kaczmarek et al. 2011). Therefore, PDBs could be a result of shearing at high differential stress and high strain rates that induced energetically-preferable slip in zircon; high temperatures in the vicinity of pseudotachylytes facilitated dislocation creep (e.g. Hobbs 1968; White 1973, 1976; Gerald et al. 1983; Ranalli 1995). Scenario c) implies formation of pseudotachylytes, followed by frictional heating of the surrounded rocks and by shearing that resulted in PDBs formation in zircon. However, differential stresses and strain rates operating in ductile shear zones are unlikely to be sufficient to form PDBs, even at elevated temperatures. Such structures have never been described in zircon from metamorphic rocks of deeper levels, derived, for example, from kimberlitic pipe (Timms et al. 2011).

Temperature regime of PDBs formation. To deform zircon crystal-plastically at high strain rates, very high temperature is required. Temperature conditions in the vicinity of frictional melts are supposed to be high, as the melt temperature has been estimated to > 1200 C, and, according to estimations done for the fault segment, approximately 97–99% of the released energy was dissipated as heat during seismic slip (Pittarello et al. 2008). These conditions may enhance migration of dislocations (Timms et al. 2012b), their accumulation in {100} planes (Leroux et al. 1999; Reddy et al. 2007), and recovery in zircon grains. However, the grains from the core of the ultramylonite zones seem to be annealed, showing very indistinct degraded planar microstructures. The local temperature in the core of the ultramylonite zone supposedly did not allow PDBs to be preserved. This is consistent with the observation that well-defined PDBs are found at the contact of ultramylonite and mylonite or at a distance of 0.5-1 mm from the ultramylonite (Fig. 1b), where the local temperature was lower than in the pseudotachylyte core.

Interrelation of PDBs with formation of other deformation structures (cataclastic and crystal-plastic)

Relative timing of multistage cataclastic deformation. The chronological sequence of the formation of microstructures in zircon is based on crosscutting relationships.

In grain 26 healed fractures do not extend into the deformed overgrowth rim (Figs. 4c and 4d, black arrows). Fractures therefore preceded rim overgrowth and crystal-plastic deformation. In grain 46 (Figs. 5i-l) the formation of a low-angle boundary together with an associated CL-bright alteration zone preceded the formation of PDBs, because the low-angle boundary limits the lateral extent of the PDBs. In grain 17 (Figs. 6a-e) healed subhorizontal fracture is offset by subvertical fractures, indicating that the latter postdated the formation of the healed fracture. Thus, healed fractures with pore traces and zones of hydrothermal alteration appearing as bright features in the CL images were formed in zircon before the formation of pseudotachylytes and ultramylonites.

On the other hand, none of the open fractures formed during the seismic activity and later on were healed or sealed. Traces of several different microstructures appear in FSE and CL images as dark lines which are not decorated by inclusions or pores and therefore are supposed to be open: i) fragmented grains (grains 03a, 10, 12, 14); ii) CFs that crosscut the metamorphic rim with crystallographic control of their spatial orientation (grain 26, upper right part); iii) fractures that limit PDBs (grains 03b and 17); iv) fractures that offset PDBs (grains 14, 45); v) CFs that are pinned by PFs (grain 21); vi) PFs (grains 43, 21, 91). We infer that healing of zircon did not occur during or after formation of pseudotachylytes, and therefore preceded PDBs formation. Formation of PDBs and cataclastic deformation, associated with seismicity and mylonitization, repeatedly alternated. For example, in grains 17 and 03b (Fig. 6) PDBs are terminated by fractures whereas in grain 14 and 45 (Fig. 7) fractures are crosscut by PDBs.

Planar fractures. So far PFs were only described from impact-related zircon grains. They are usually parallel to {001}, {100}, {111}, {201}, {211} and {221} planes in zircon crystal lattice (Leroux et al. 1999; Timms et al. 2012b; Erickson et al. 2013a). Erickson et al. (2013a) reported about frequent occurrence of {100} orientation of PFs, and their relatively early development. PFs parallel to zircon {100} planes form at the first stage of shock deformation and are most easily annealed afterwards (Erickson et al. 2013a). That points to comparatively easy activation of these planes in the zircon crystal lattice. In our study we identified PFs tracing parallel to {100} planes, often overprinting PDBs. Their spatial relationships indicate that PDBs act as a structural precursor for PFs; both structures likely form as a result of one process and may represent different evolutionary stages of the same structure. We suggest that PFs can overprint PDBs in segments of high dislocation density. The possibility that low-angle boundaries could evolve to form PFs is suggested by Erickson et al. (2013a).

In grain 21 PFs are not associated with PDBs. In that case PFs could represent “micro-cleavage” in {100} planes, generated by high shear stresses as described with shock experiments of Leroux et al. (1999).

Curviplanar fractures. “Non-planar” or “Curviplanar fractures” are interpreted as impact- or seismic-related structures (Austrheim and Corfu 2009; Cavosie et al. 2010; Moser et al. 2011;

Timms et al. 2012b; Erickson et al. 2013a). They represent "broadly parallel, spaced, and curved" fractures (Moser et al. 2011) and are supposed to result from shock deformation. The CFs in grains 03b, 17, 26 are not related to seismic activity and formed earlier than planar microstructures. CFs appear as regular fractures resulting from cataclastic deformation. They may or may not be healed and have broadly parallel orientation due to crystal internal heterogeneities (for example, growth zoning, crystallographic anisotropy), or due to specific grain shape- or crystallographic orientation in the local stress field. For example, open CFs described in grain 26 are roughly parallel to the crystallographic plane {100} and, moreover, parallel to the growth zoning; the healed CFs are roughly parallel to the plane {331} (Fig. 4c, white and black arrows correspondingly). In grain 21 CFs are parallel to {011}. In the study of Kaczmarek et al. (2011) CFs appear to be a result on deformation in a ductile shear zone.

We suggest that CFs cannot be used as a reliable indicator of seismic activity or shock deformation, as they can be easily formed during other deformation processes in the crust. An argument for CFs formation during shock deformation could be the observation of impact melt filling CFs (Moser et al. 2011), but even then CFs might only represent reactivated preexisting fractures (Erickson et al. 2013a).

Crystal-plastic deformation (besides PDBs) and associated fragmentation at the margins. Crystal-plastic deformation in zircon is characterized by lattice distortion due to formation and migration of geometrically necessary dislocations (Reddy et al. 2007) and has been documented for different geological settings: syn-magmatic deformation (Reddy et al. 2009; Timms and Reddy 2009; MacDonald et al. 2013), deformation in ductile shear zones (Kaczmarek et al. 2011; Piazolo et al. 2012; Kovaleva et al. 2014), impact-related lattice distortion (Leroux et al. 1999; Moser et al. 2009; Nemchin et al. 2009; Timms et al. 2012b; Grange et al. 2013).

Lattice distortion, preserved by some fragments of grain 12 (Fig. 3a), indicates that crystal-plastic deformation preceded the fragmentation of this grain. Thus, fragmentation of zircon, together with rock faulting, should be a later and lower-temperature process. The lattice distortion pattern of grain 26 (Fig. 4) resembles that observed in zircon from ductile shear zones (e.g. Reddy et al. 2007; Piazolo et al. 2012; Kovaleva et al. 2014). Marginal grain fragmentation observed in the domain (i) indicates that the differential stress increases towards the rim of the grain (Kenkmann 2000; Kovaleva et al. 2014). Deformation structures of the domain (i) are consistent with lattice distortion type (II), whereas domain (ii) can be classified as distortion pattern type (I) (Piazolo et al. 2012; Kovaleva et al. 2014). The distortion patterns in zircon from the IVZ shear zone are similar those from other ductile shear zones in different tectonic settings (e.g. Reddy et al. 2007; Piazolo et al. 2012; Kovaleva et al. 2014), where formation of pseudotachylytes has not been documented. However, the content of grains with lattice distortion in ultramylonites is 2-3 times higher than in host mylonites. Most likely, crystal-plastic deformation results from shearing and mylonitization of the host rocks during ultramylonite formation, and not necessarily related to seismic events.

Crystal-plastic deformation observed in grain 14 (Figs. 7a-c) likely overprinted PDBs, which were formed earlier; it looks like PDBs are slightly bending in plastically-deformed domains. In grain 45, the relative timing of crystal-plastic deformation and formation of PDBs is questionable.

Implications for the evolution of the IVZ

Multiple crosscutting relationships indicate that brittle and crystal-plastic deformation as well as formation of planar microstructures in zircon occurred coherently, but in different succession for each grain that is shown in the schematic sketch (Fig. 11a). Thus, our data support the scenario of IVZ tectono-metamorphic evolution suggested by Pittarello et al. (2012). Non-hydrous restitic rocks of the lower crustal granulite-facies section were supposed to be exhumed into the seismically active zone. Earthquakes caused frictional melting immediately followed by mylonitization localized at structural heterogeneities (Pennacchioni and Mancktelow 2007) under amphibolite facies conditions. Ultramylonite formation overprinted pseudotachylytes; cycle of fracturing, melting and mylonitization could be repeated several times in the same shear zone during a single tectono-metamorphic event (Pittarello et al. 2012).

Grain fragmentation and the formation of related transgranular faults likely occurred soon after the formation of pseudotachylytes and ultramylonites. The distribution of fragmented zircon grains frames ultramylonites (Fig. 1b, grains 04a and 10); and the faults hosting fragmented grains crosscut and offset ultramylonites and pseudotachylytes. Zircon grains within ultramylonites do not experience intensive fragmentation, presumably because the temperature in these zones remained higher.

Implications

This study demonstrates that planar microstructures in zircon are not restricted to shock-induced PDFs and PFs, are not exclusively evidence of shock metamorphism, but can also form in the Earth's crust as a result of seismic activity. Furthermore, PDBs in zircon could be a newly identified indicator of seismic activity/earthquakes besides of pseudotachylytes.

Deformation microstructures as PDBs could change trace element composition in zircon and enhance partial- or complete resetting of zircon isotopic systems (e.g. Reddy et al. 2006;

Timms et al. 2006, 2011, 2012b; Timms and Reddy 2009; Moser et al. 2009, 2011; Piazolo et al. 2012; MacDonald et al. 2013), thus making possible to date paleo-seismic events directly.

On the other hand, new data provides the link between seismology, mineral physics and metamorphic petrology combined with structural geology; demonstrates how closely seismic and metamorphic processes were interacting in the IVZ rocks; and gives an example how in particular the released seismic energy at depth influences petrophysical properties of the deep crust.

Acknowledgments

This study was funded by the University of Vienna (doctoral school “DOGMA”, project IK 052) and the Austrian Science Foundation Fund (FWF): I471-N19, which is part of the DFG-FWF funded international research group FOR741-DACH.

The authors are grateful to Christian Auer, Claudia Beybel, Franz Biedermann, Aaron Cavosie, Sigrid Hrabe, Matthew Huber, Lidia Pittarello, Claudia Trepmann, and all colleagues of the FOR741 research group for fruitful discussions and the Geologische Bundesanstalt (GBA) of Austria for access to the SEM.

References cited

Akaogi, M. and Navrotsky, A. (1984) The quartz—coesite—stishovite transformations: new calorimetric measurements and calculation of phase diagrams. Physics of the Earth and Planetary Interiors, 36, 124-134.

Angiboust, S., Agard, P., Yamato, P., Raimbourg, H. (2012) Eclogite breccias in a subducted ophiolite: a record of intermediate-depth earthquakes? Geology, 40, 707-710.

Austrheim, H. (2013) Fluid and deformation induced metamorphic processes around Moho beneath continent collision zones: Examples from the exposed root zone of the Caledonian mountain belt, W-Norway. Tectonophys, 609, 620-635.

Austrheim, H. and Corfu, F. (2009) Formation of planar deformation features (PDFs) in zircon during coseismic faulting and an evaluation of potential effects on U–Pb systematics. Chemical Geology, 261, 25–31.

Austrheim, H., Erambert, M., Boundy T.M. (1996) Garnet recording deep crustal earthquakes. Earth and Planetary Science Letters. 139, 223-238.

Bohor, B.F., Betterton, W.J., and Krogh, T.E. (1993) Impact-shocked zircons: discovery of shock-induced textures reflecting increasing degrees of shock metamorphism. Earth and Planetary Science Letters, 119, 419-424.

Brodie, K.H., Rutter, E.H., and Evans, P. (1992) On the structure of the Ivrea-Verbano Zone (northern Italy) and its implications for present-day lower continental crust geometry. Terra Nova, 4, 34-39.

Cavosie, A.J., Quintero, R.R., Henri A. Radovan, H.A., and Moser, D.E. (2010) A record of ancient cataclysm in modern sand: Shock microstructures in detrital minerals from the Vaal River, Vredefort Dome, South Africa. Geological Society of America Bulletin, 122, 1968-1980.

Chen, Y.D., O'Reilly, S.Y., Kinny, P.D., Griffin, W.L. (1994) Dating lower crust and upper mantle events: an ion microprobe study of xenoliths from kimberlitic pipes, South Australia. Lithos 32, 77–94.

Corfu, F., Hanchar, J.M., Hoskin P.W.O., and Kinny, P. (2003) Atlas of zircon textures. In: J.M. Hanchar, P.W.O. Hoskin, Eds., Zircon, p. 468-500. Mineralogical Society of America and Geochemical Society, Reviews in Mineralogy and Geochemistry, 53, Washington D.C.

Erickson, T.M., Cavosie, A.J., Moser, D.E., Barker, I.R., and Radovan, H.A. (2013a) Correlating planar microstructures in shocked zircon from the Vredefort Dome at multiple scales: Crystallographic modeling, external & internal imaging, and EBSD structural analysis. American Mineralogist, 98, 53-65.

Erickson, T.M., Cavosie, A.J., Moser, D.E., Barker, I.R., Radovan, H.A., and Wooden, J. (2013b) Identification and provenance determination of distally transported, Vredefort-derived shocked minerals in the Vaal River, South Africa using SEM and SHRIMP-RG techniques. Geochimica et Cosmochimica Acta, 107, 170-188.

Gerald, F.J.D., Etheridge, M.A., and Vernon, R.H. (1983) Dynamic recrystallization in a naturally deformed albite. Textures and Microstructures, 5, 219-237.

Grange, M.L., Pidgeon, R.T., Nemchin, A.A., Timms, N.E., and Meyer, C. (2013) Interpreting U–Pb data from primary and secondary features in lunar zircon. Geochimica et Cosmochimica Acta, 101, 112–132.

Hobbs, B.E. (1968) Recrystallization of single crystals of quartz. Tectonophysics, 6, 353-401.

Kaczmarek, M.A., Reddy, S.M., and Timms, N.E. (2011) Evolution of zircon deformation mechanisms in a shear zone (Lanzo massif, Western-Alps). Lithos, 127, 414-426.

Kalleson, E., Corfu, F., and Dypvik, H. (2009) U–Pb systematics of zircon and titanite from the Gardnos impact structure, Norway: Evidence for impact at 546 Ma? Geochimica et Cosmochimica Acta, 73, 3077–3092.

Kamo, S.L., Reimold, W.U., Krogh, T.E., and Colliston, W.P. (1996) A 2.023 Ga age for the Vredefort impact event and a first report of shock metamorphosed zircons in pseudotachylitic breccias and granophyre. Earth and Planetary Science Letters, 144, 369–387.

Khazanehdari, J., Rutter, E.H., Brodie K.H. (2000) High-pressure-high-temperature seismic velocity structure of the midcrustal and lower crustal rocks of the Ivrea-Verbano zone and Serie dei Laghi, NW Italy. Journal of Geophysical Research, 105, 13843-13858.

Kenkmann, T. (2000) Processes controlling the shrinkage of porphyroclasts in gabbroic shear zones. Journal of Structural Geology, 22, 471-487.

Klötzli, U.S., Sinigoi, S., Quick, J.E., Demarchi, G., Tassinari, C.C.G., Sato, K., and Günes, Z. (2014) Duration of igneous activity in the Sesia Magmatic System and implications for high-temperature metamorphism in the Ivrea–Verbano deep crust. Lithos, 206–207, 19–33.

Kovaleva, E., Klötzli, U., Habler, G., and Libowitzky, E. (2014) Finite lattice distortion patterns in plastically deformed zircon grains. Solid Earth, 5, 1099-1122.

Kresten, P., Fels, P., Berggren, G. (1975) Kimberlitic zircons— a possible aid in prospecting for kimberlites. Mineralium Deposita, 10, 47–56.

Leroux, H., Reimold, W.U., Koeberl, C., Hornemann, U., and Doukhan, J.C. (1999) Experimental shock deformation in zircon: a transmission electron microscopic study. Earth and Planetary Science Letters, 169, 291–301.

Lund, M.G. and Austrheim, H. (2003) High-pressure metamorphism and deep-crustal seismicity: evidence from contemporaneous formation of pseudotachylytes and eclogite facies coronas. Tectonophysics, 372, 59–83.

MacDonald, J.M., Wheeler, J., Harley, S.L., Mariani, E., Goodenough, K.M., Crowley, Q., and Tatham, D. (2013) Lattice distortion in a zircon population and its effects on trace element mobility and U–Th–Pb isotope systematics: examples from the Lewisian Gneiss Complex, northwest Scotland. Contributions to Mineralogy and Petrology, 166, 21–41.

Moser, D.E., Davis, W.J., Reddy, S.M., Flemming, R.L., and Hart, R.J. (2009) Zircon U–Pb strain chronometry reveals deep impact-triggered flow. Earth and Planetary Science Letters, 277, 73–79.

Moser, D.E., Cupelli, C.L., Barker, I.R., Flowers, R.M., Bowman, J.R., Wooden, J., and Hart, J.R. (2011) New zircon shock phenomena and their use for dating and reconstruction of large impact structures revealed by electron nanobeam (EBSD, CL, EDS) and isotopic U–Pb and (U–Th)/He analysis of the Vredefort dome. Canadian Journal of Earth Sciences, 48, 117–139.

Nemchin A., Timms N.E., Pidgeon R., Geisler T., Reddy S.M., and Meyer C. (2009) Timing of crystallization of the lunar magma ocean constrained by the oldest zircon. Nature Geoscience, 2, 133-136.

Öpik, E.J., (1958) Meteor impact on solid surface. Irish Astronomical Journal, 5, 14-33.

Passchier, C.W. (1982) Mylonitic deformation in the Saint-Barthélemy massif, French Pyrenees, with emphasis on the genetic relationship between ultramylonite and pseudotachylyte, 173 p. Ph.D. thesis, University of Amsterdam, Amsterdam.

Pennacchioni, G. and Mancktelow, N.S. (2007) Nucleation and initial growth of a shear zone network within compositionally and structurally heterogeneous granitoids under amphibolite facies conditions. Journal of Structural Geology, 29, 1757-1780.

Piazolo, S., Austrheim, H., and Whitehouse, M. (2012) Brittle-ductile microfabrics in naturally deformed zircon: Deformation mechanisms and consequences for U-Pb dating. American Mineralogist, 97, 1544–156.

Pidgeon R., Nemchin A., and Kamo S.L. (2011) Comparison of structures in zircons from lunar and terrestrial impactites. Canadian Journal of Earth Sciences, 48, 107–116.

Pittarello, L., Di Toro, G., Bizzarri, A., Pennacchioni, G., Hadizadeh, J., and Cocco, M. (2008) Energy partitioning during seismic slip in pseudotachylyte-bearing faults (Gole Larghe Fault, Adamello, Italy). Earth and Planetary Science Letters, 269, 131–139.

Pittarello, L., Pennacchioni, G., and Di Toro, G. (2012) Amphibolite-facies pseudotachylytes in Premosello metagabbro and felsic mylonites (Ivrea Zone, Italy). Tectonophysics, 580, 43–57.

Quick, J.E., Sinigoi, S., Peressini, G., Demarchi, G., Wooden, J.L., and Sbisà, A. (2009) Magmatic plumbing of a large Permian caldera exposed to a depth of 25 km. Geology, 37, 603-606.

Ranalli, G. (1995) Rheology of the Earth, 2nd ed., 413 p. Chapman & Hall, London.

Reddy, S.M. and Buchan, C. (2005) Constraining kinematic rotation axes in high-strain zones: a potential microstructural method? In: D. Gapais, J.P. Brun, P.R. Cobbold, Eds., Deformation Mechanisms, Rheology and Tectonics: from Mineral to the Lithosphere, 18, p. 1-10. Geological Society Special Publications, 243, London.

Reddy, S.M., Timms, N.E., Trimby, P., Kinny, P.D., Buchan C., and Blake K. (2006) Crystal-plastic deformation of zircon: a defect in the assumption of chemical robustness. Geology, 34, 257-260.

Reddy, S.M., Timms, N.E., Pantleon, W., and Trimby, P. (2007) Quantitative characterization of plastic deformation of zircon and geological implications. Contributions to Mineralogy and Petrology, 153, 625–645.

Redler, C., Johnson, T.E., White R.W., and Kunz, B.E. (2012) Phase equilibrium constraints on a deep crustal metamorphic field gradient: metapelitic rocks from the Ivrea Zone (NW Italy). Journal of Metamorphic Geology, 30, 235–254.

Rudnick, R.L. and Williams, I.S. (1987) Dating of lower crust by ion microprobe. Earth and Planetary Science Letters 85, 145–163.

Rutter, E.H., Brodie K.H., James T., and Burlini L. (2007) Large-scale folding in the upper part of the Ivrea-Verbano zone, NW Italy. Journal of Structural Geology, 29, 1-17.

Sibson, R.H. (1975) Generation of pseudotachylyte by ancient seismic faulting. Geophysical Journal of the Royal Astronomical Society, 43, 775–794.

Sinigoi, S., Quick, J.E., Demarchi, G., and Klötzli, U. (2011) The role of crustal fertility in the generation of large silicic magmatic systems triggered by intrusion of mantle magma in the deep crust. Contributions to Mineralogy and Petrology, 162, 691-707.

Spudich, P., Guatteri, M., Otsuki, K., Minagawa, J. (1998) Use of fault striations and dislocations models to infer tectonic shear stress during the 1995 Hyogo-ken (Kobe) earthquake. Bulletin of the Seismological Society of America, 88, 413–427.

Techmer, K.S., Ahrendt, H., and Weber, K. (1992) The development of pseudotachylyte in the Ivrea-Verbano Zone of the Italian Alps. Tectonophysics, 204, 307–322.

Timms, N.E. and Reddy, S.M. (2009) Response of cathodoluminescence to crystal-plastic deformation in zircon. Chemical Geology, 261, 11–23.

Timms, N.E., Kinny, P., and Reddy, S.M. (2006) Enhanced diffusion of uranium and thorium linked to crystal plasticity in zircon. Geochemical Transactions, 7, 10.

Timms, N.E., Kinny, P., Reddy, S.M., Evans K., Clark C., Healy D. (2011) Relationship among titanium, rare earth elements, U–Pb ages and deformation microstructures in zircon: Implications for Ti-in-zircon thermometry. Chemical Geology 280, 33–46.

Timms, N.E., Reddy, S.M., Fitz Gerald, J.D., Green, L., Muhling, J.R. (2012a) Inclusion-localised crystal-plasticity, dynamic porosity, and fast-diffusion pathway generation in zircon, Journal of Structural Geology, 35, 78-89.

Timms, N.E., Reddy, S.M., Healy, D., Nemchin, A.A., Grange, M.L., Pidgeon, R.T., and Hart, R. (2012b) Resolution of impact-related microstructures in lunar zircon: A shock-deformation mechanism map. Meteoritics and Planetary Science, 47, 120–141.

Thomson, O.A., Cavosie, A. J., Moser, D.E., Barker, I., Radovan, H.A., and French, B.M. (2014) Preservation of detrital shocked minerals derived from the 1.85 Ga Sudbury impact structure in modern alluvium and Holocene glacial deposits. Geological Society of America Bulletin, 126, 720-737.

Wheeler, J., Mariani, E., Piazolo, S., Prior, D.J., Trimby, P., and Drury, M.R. (2009) The Weighted Burgers Vector: a new quantity for constraining dislocation densities and types using Electron Backscatter Diffraction on 2D sections through crystalline materials. Journal of Microscopy, 233, 482-494.

White, S. (1973) Syntectonic recrystallization and texture development in quartz. Nature, 244, 276-278.

White, S. (1976) The effects of strain and microstructure fabrics and deformation mechanisms in quartzite. Philosophical Transactions of the Royal Society of London, 283, 69-86.

Yang, J.-J., Fan, Z.-F., Yu, C., Yan, R. (2014a) Coseismic formation of eclogite facies cataclasite dykes at Yangkou in Chinese Su-Lu UHP metamorphic belt. Journal of Metamorphic Geology, 32, 937-960.

Yang, J.-J., Huang, M.-X., Wu, Q.-Y., Zhang, H.-R. (2014b). Coesite-bearing eclogite breccia: implications for coseismic ultrahigh-pressure metamorphism and the rate of the process. Contributions to Mineralogy and Petrology. 167, 1013-1030.

Figure captions

Figure 1. (a) Field photograph of the sampled outcrop, sampled site is indicated by arrow. (**b**) Plain polarized transmitted light photograph of the thin section with shear zone (dark area). *Grt* = garnet. Axes show orientation of thin section in the sample reference frame. Labels with numbers are locations of the analyzed zircon grains.

Figure 2. Pseudotachylyte veins (orientation as in Fig. 1b). *Pl* = plagioclase, *Grt* = garnet, *Ilm* = ilmenite, *Bt* = biotite. (**a**) Plane-polarized transmitted light photomicrograph, black veins

are pseudotachylytes hosted by ultramylonite. (**b**) BSE image of the area marked in Figure 2a. Pseudotachylyte vein with bright rim due to garnet enrichment in contact with ultramylonite. (**c**) BSE image of pseudotachylyte vein in detail. (**d**) BSE image of the rim of pseudotachylyte vein. (**e**) Enlarged area from 2d with needle-shaped fine grains, resembling microlites. (**f**) Reflected light photomicrograph. The pseudotachylyte vein has a garnet rim (bright), separating it from the host ultramylonite. (**g**) BSE image of the pseudotachylyte vein shown in 2f, offset by a fracture zone.

Figure 3. Fragmented zircon grains. Axes show the sample reference frame. (**a**) Orientation contrast (FSE) image of grain 12. (**b**) CL image of grain 12. (**c**) Orientation contrast image of grain 04a. (**d**) Orientation contrast image of grain 10, black dashed line contours the zircon grain. (**e**) BSE image of the grain 10.

Figure 4. Grain 26 revealing evidence of crystal-plastic deformation. (**a**) EBSD map color coded for zircon misorientation with respect to a reference point (red star marker). Arrows indicate fragments detached from a parent grain. Inset: pole figure plot showing zircon crystal directions (lower hemisphere equal area projection) of the grain portion ii, color coded as in Figure 4a. Labels indicate the crystallographic directions. Plot shows scattering of axes due to rotation around [001] (red circle), indicated by black arrows. (**b**) EBSD pattern quality map of zircon area i, showing boundaries colored for misorientation angles. (**c**) Orientation contrast image, arrows indicate curviplanar fractures (CFs), black – healed, white – open. (**d**) CL image, arrows as in 4c.

Figure 5. Grains with planar deformation bands (PDBs). (**a**) Orientation contrast image of grain 34. (**b**) CL image of grain 34. (**c**) EBSD orientation deviation map of grain portion highlighted in Figure 5a, color coded for zircon misorientation with respect to a reference point

(red star marker). Dashed circle highlights thickening of the PDBs at intersection site. (**d**) Pole figure plot showing zircon crystal directions of the grain portion shown in 5c. Labels indicate the crystallographic directions. Black lines are orientations of PDBs traces, red dashed lines are the reconstruction of PDBs orientation. (**e**) Orientation contrast image of grain 43. Black arrows highlight planar fractures (PFs) aligned in array of segments with double-wings, enlarged in upper right inset. (**f**) CL image of grain 43. Dark rectangular area represents the position of the EBSD map. (**g**) EBSD orientation deviation map of grain portion highlighted in 5e, color coded for zircon misorientation with respect to a reference point. Dashed circles same as in 5c. White arrow indicates the position of misorientation profile, shown in Figure 9a, numbers are intersections with PDBs, shown in Figure 9a. (**h**) Pole figure plot showing zircon crystal directions of the grain portion shown in 5g, lines as in 5d. (**i**) Orientation contrast image of grain 46. Black arrow indicates low-angle boundary. (**j**) CL image of grain 46. Black arrow shows low-angle boundary, white arrow highlights bright CL-band. (**k**) EBSD orientation deviation map of the grain portion highlighted in 5i, black arrow as in 5i. (**l**) Pole figure plot showing zircon crystal directions of the grain portion shown in 5k, black and red lines as in 5d, blue line gives approximate orientation of low-angle boundary.

Figure 6. Grains with PDBs and brittle fractures. (**a**) Orientation contrast image of grain 17. Arrows indicate PFs. (**b**) Plain-polarized transmitted light photomicrograph of the grain 17, parallel lamellae are present in the lower right portion (direction indicated by white arrows), PF is indicated by black arrow. (**c**) Pole figure plot showing zircon crystallographic directions (labeled) of grain 17, color coding as in Figure 6d. PDBs trace orientations (white lines) and their reconstructed plane (red dashed line). (**d**) EBSD orientation deviation map of grain 17, color coded for zircon misorientation with respect to a reference point. White arrow indicates the position of misorientation profile, shown in Figure 9b, numbers are intersections with PDBs,

shown in Figure 9b. (**e**) CL image of grain 17. (**f**) Orientation contrast image of grain 03b. (**g**) CL image of the grain 03b. (**h**) EBSD orientation deviation map of the domain highlighted in 6f, color coded for misorientation relative to a reference point. Black arrow indicates the position of the misorientation profile, shown in Figure 9c, numbers are intersections with PDBs, shown in 9c. (**i**) Pole figure plot showing zircon crystallographic directions (labeled) of the domain shown in 6h. PDBs trace orientations are marked by black lines and their reconstructed planes by red dashed lines.

Figure 7. Grains showing crystal-plastic- and brittle deformation features and PDBs. (**a**) Orientation contrast image of grain 14. (**b**) CL image of grain 14. (**c**) EBSD orientation deviation map of grain 14 color coded for zircon misorientation with respect to a reference point (red star marker). Red dashed line shows offset of PDBs. (**d**) Orientation contrast image of grain 45. Red arrow indicates domain with crystal-plastic deformation. (**e**) CL image of grain 45. (**f**) EBSD orientation deviation map of grain portion indicated in 7d and 7e, color coded for zircon misorientation with respect to a reference point.

Figure 8. Grains with PFs. (**a**) Orientation contrast image of grain 21. black arrows indicate PFs, white arrows – CFs, grey arrows – spots, where the CFs are terminated by PFs. (**b**) CL image, black arrow highlights position of PF. (**c**) Pole figure plot showing zircon crystal directions of grain 21. PDBs trace orientation is marked by thick line and its reconstructed plane by dashed line. (**d**) Plane-polarized transmitted light photomicrograph of grain 21, dark parallel lamellae are highlighted by arrows and represent PFs. (**e**) Orientation contrast image of grain 91 embedded in epoxy resin. Arrows indicate PFs parallel to PDBs. (**f**) CL image of grain 91, arrow indicates PF.

Figure 9. Misorientation profiles across zircon grains with PDBs. Gray line indicates misorientation between neighboring points; black line indicates misorientation relative to the starting point. Numbers mark misorientation peaks in the profiles that correspond to PDBs. (**a**) Grain 43, position of the profile is shown in Figure 5g. (**b**) Grain 17, position of the profile is shown in Fig. 6D. (**c**) Grain 03b, position of the profile is shown in Figure 6h.

Figure 10. EBSD pattern quality maps with superimposed Weighted Burgers Vector (WBV) components for the highlighted rectangular subareas. The three numbers, listed for each subarea, are the *a*, *b* and *c* components of WBV, measured in $(\mu m)^{-2}$. Numbers were derived with the MATLAB toolbox CrystalScape 1.3 (Wheeler et al., 2009). Rectangles with grey lines show the areas with WBV that is comparatively low with respect to the rest of the mapped area. Dotted lines show rectangle areas with WBV dominated by *a* component, dashed lines – by *b* component, white lines – dominated by *c* component, black solid lines show areas with WBV with mixed components. (**a**) Grain 34. (**b**) Grain 43. (**c**) Grain 46. (**d**) Grain 03a.

Figure 11. (a) Scenarios for zircon microstructural evolution in the IVZ (schematic sketch), summarizing microstructures observed in this study. Chronological sequence for microstructures reconstructed is based on crosscutting relationships. (**b**) Crystallographic orientations of the <001> and <100> axes of the zircon grains with PDBs from thin section shown in Figure 1b. Circles show data from grains with one (open) or two (filled) resolved sets of PDBs. 6 of 8 grains (75 %) have the c-axis approximately orientation normal to thin section plane (Y-Z plane).

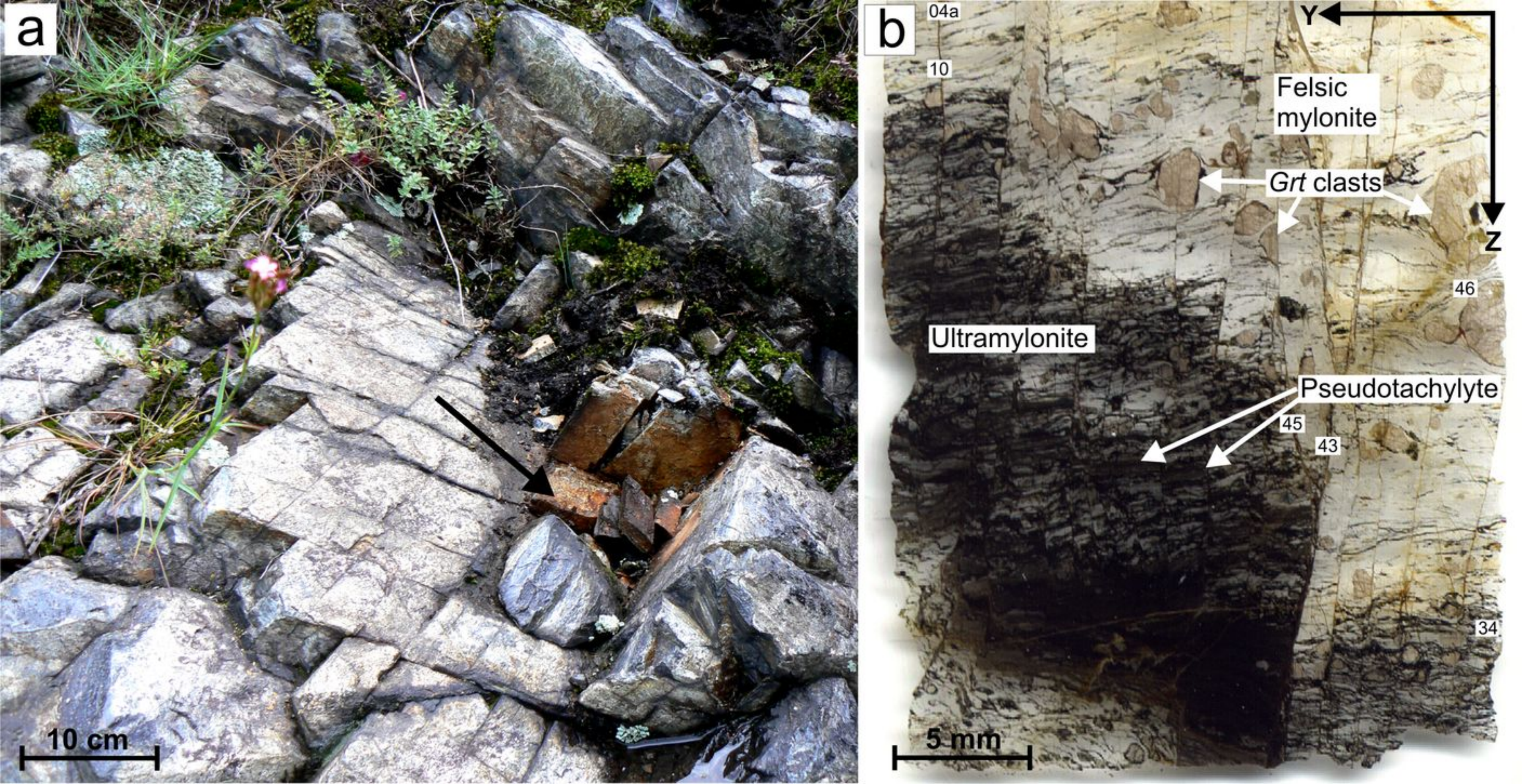
a
10 cm
b
04a
10
Y
Z
Felsic mylonite
Grt clasts
46
Ultramylonite
Pseudotachylyte
45
43
34
5 mm

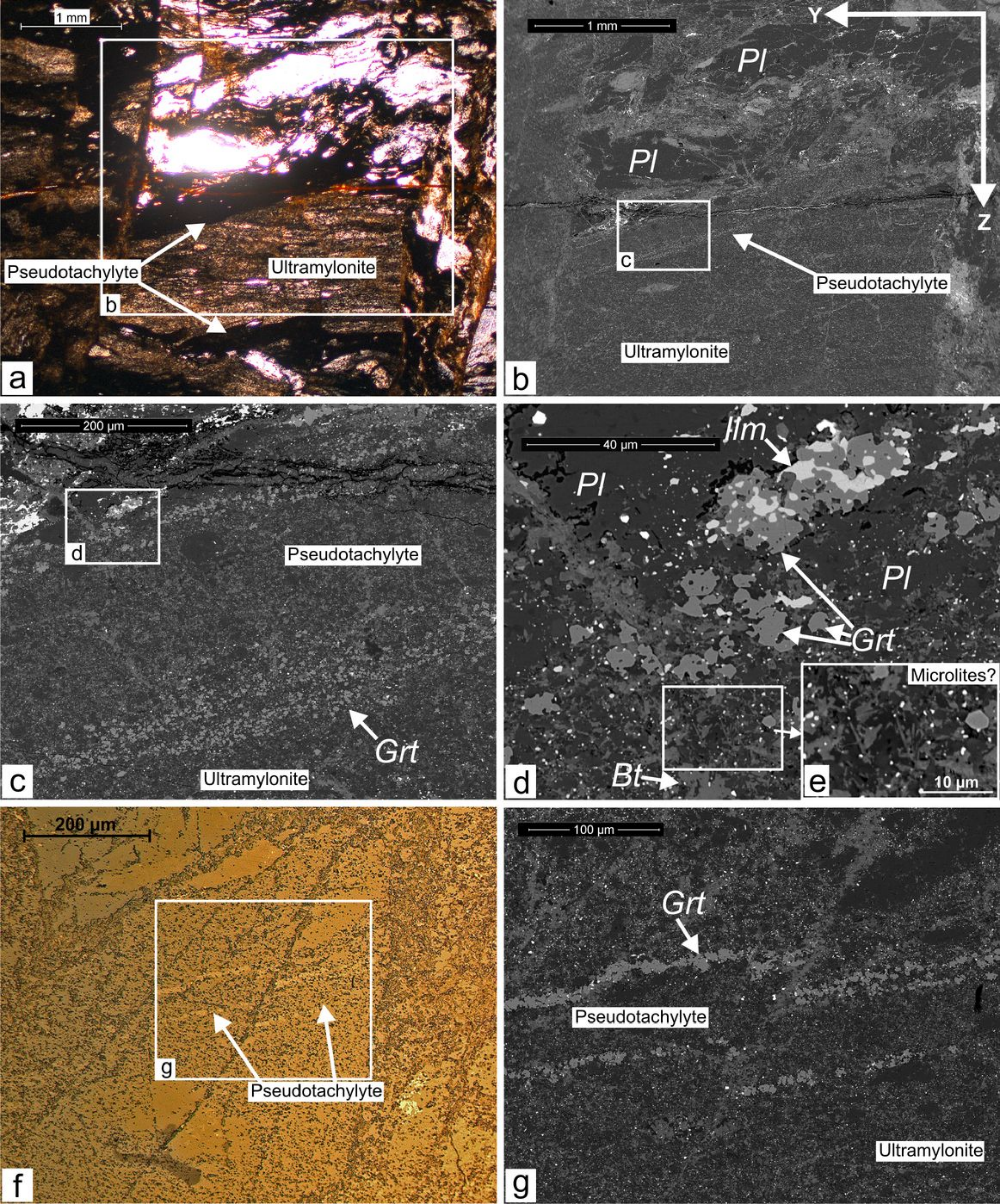
1 mm
Pseudotachylyte
Ultramylonite
b
a
1 mm
Y
Z
Pl
Pl
c
Pseudotachylyte
Ultramylonite
b
200 µm
d
Pseudotachylyte
Grt
Ultramylonite
c
40 µm
Ilm
Pl
Pl
Grt
Microlites?
Bt
10 µm
d
e
200 µm
g
Pseudotachylyte
f
100 µm
Grt
Pseudotachylyte
Ultramylonite
g

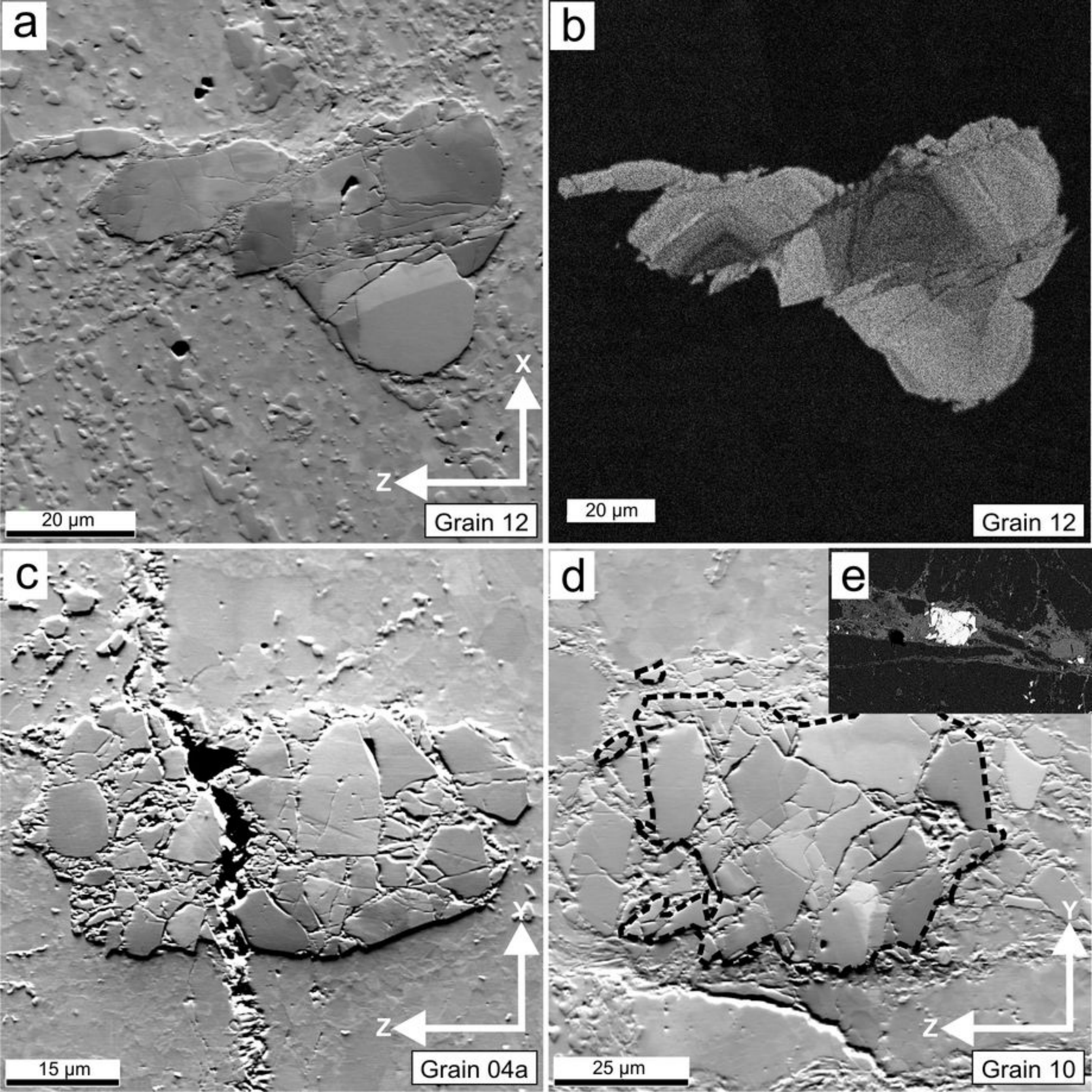
a
X
Z
20 µm
Grain 12
b
20 µm
Grain 12
c
X
Z
15 µm
Grain 04a
d
e
Y
Z
25 µm
Grain 10

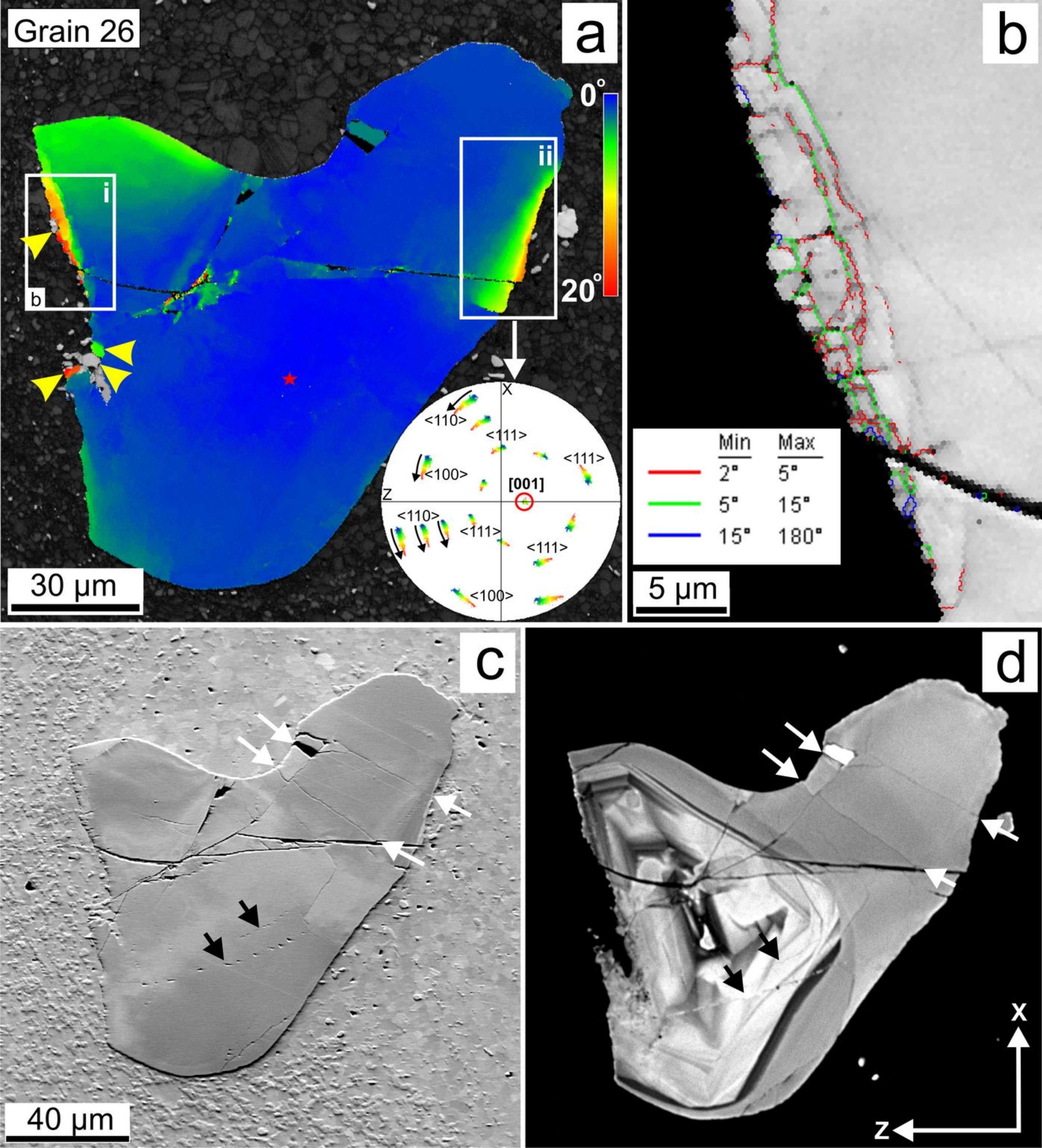
Grain 26
a
0°
20°
i
ii
b
[001]
X
Z
<110>
<111>
<100>
<111>
<110>
<111>
<111>
<100>
30 µm
b
Min Max
2° 5°
5° 15°
15° 180°
5 µm
c
40 µm
d
X
Z

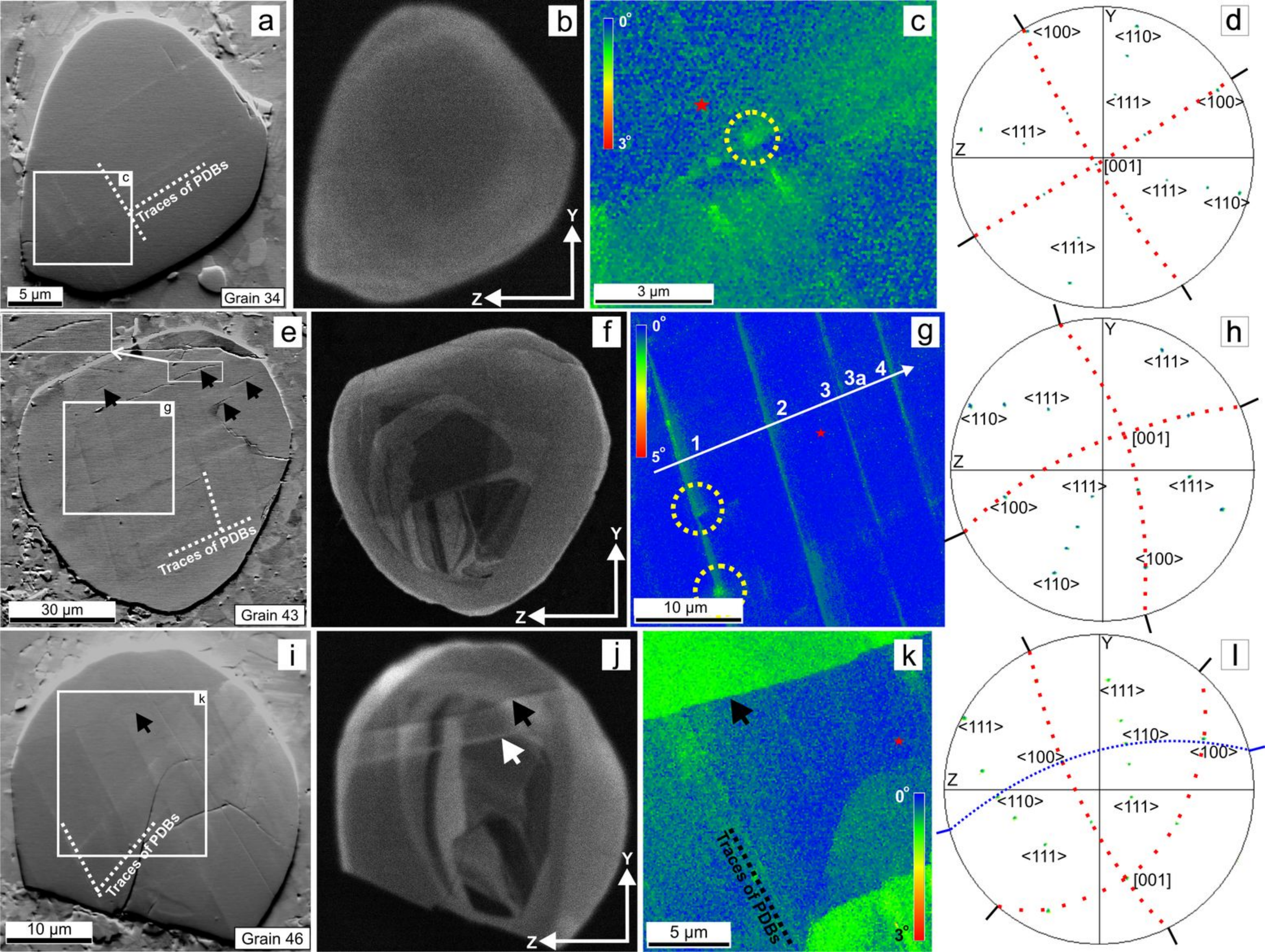
a
c
Traces of PDBs
5 µm
Grain 34
b
Y
Z
c
0°
3°
3 µm
d
Y
Z
<100>
<110>
<111>
<111>
<100>
<111>
[001]
<111>
<110>
<111>
e
g
Traces of PDBs
30 µm
Grain 43
f
Y
Z
g
0°
5°
1
2
3
3a
4
10 µm
h
Y
Z
<111>
<111>
<110>
[001]
<100>
<111>
<111>
<100>
<110>
i
k
Traces of PDBs
10 µm
Grain 46
j
Y
Z
k
Traces of PDBs
0°
3°
5 µm
l
Y
Z
<111>
<111>
<110>
<100>
<100>
<110>
<111>
<111>
[001]

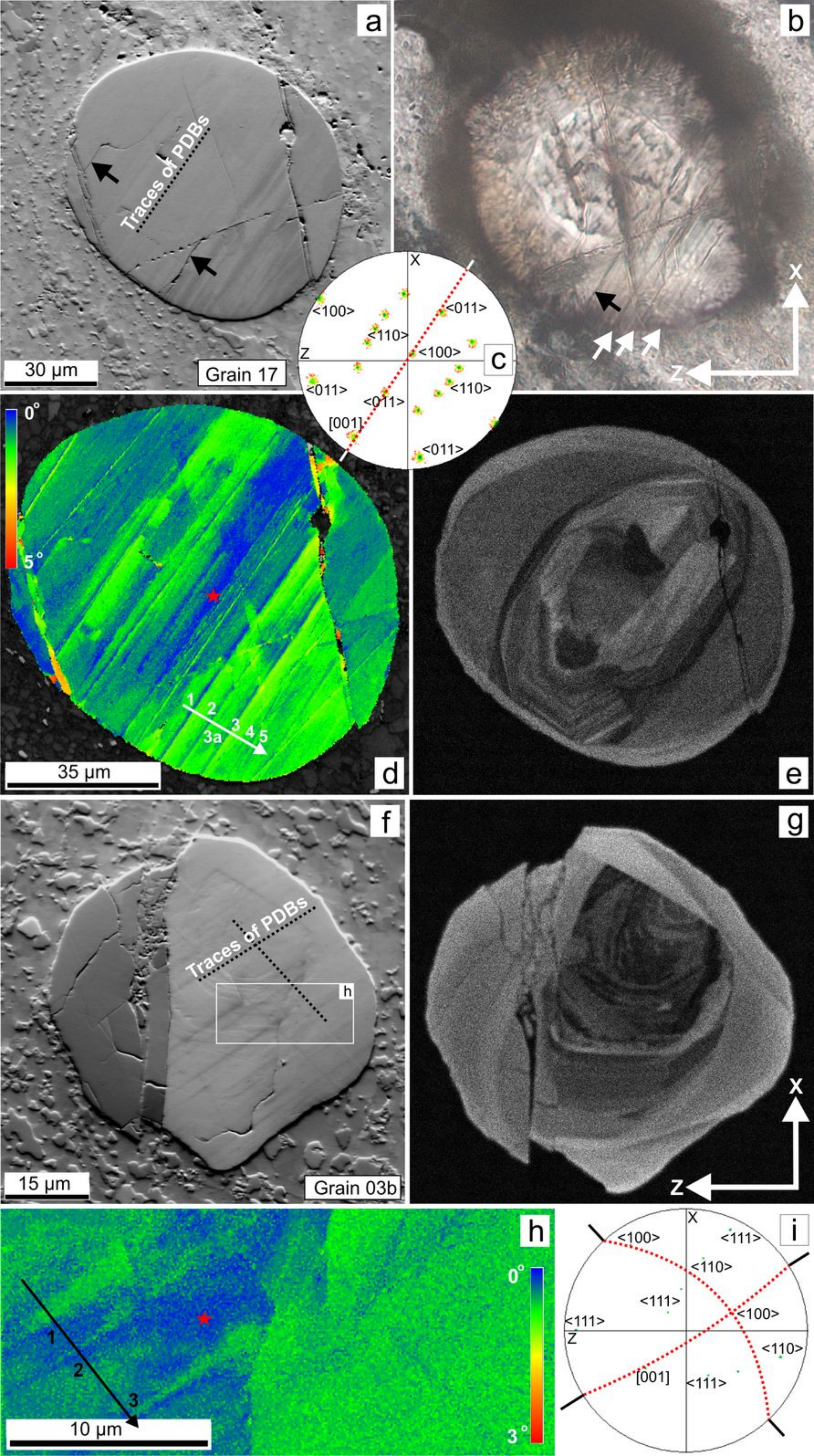
a
Traces of PDBs
30 µm
Grain 17
b
X
Z
c
X
Z
<100>
<011>
<110>
<100>
<011>
<110>
<011>
[001]
<011>
d
0°
5°
1
2
3
3a
4
5
35 µm
e
f
Traces of PDBs
h
15 µm
Grain 03b
g
X
Z
h
0°
3°
1
2
3
10 µm
i
X
<100>
<111>
<110>
<111>
<111>
<100>
Z
<110>
[001]
<111>

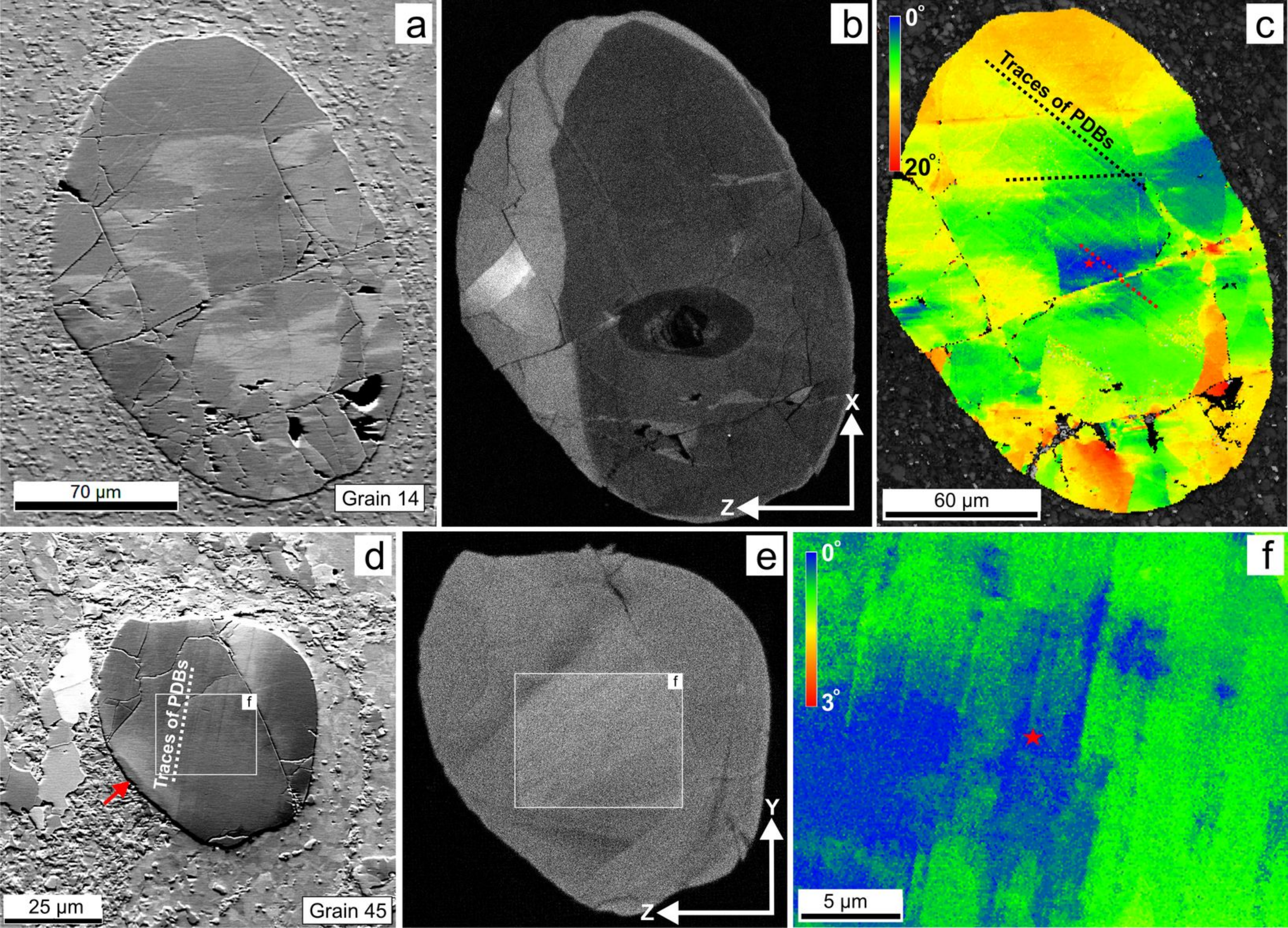
a
70 μm
Grain 14
b
X
Z
c
0°
20°
Traces of PDBs
60 μm
d
Traces of PDBs
f
25 μm
Grain 45
e
f
Y
Z
f
0°
3°
5 μm

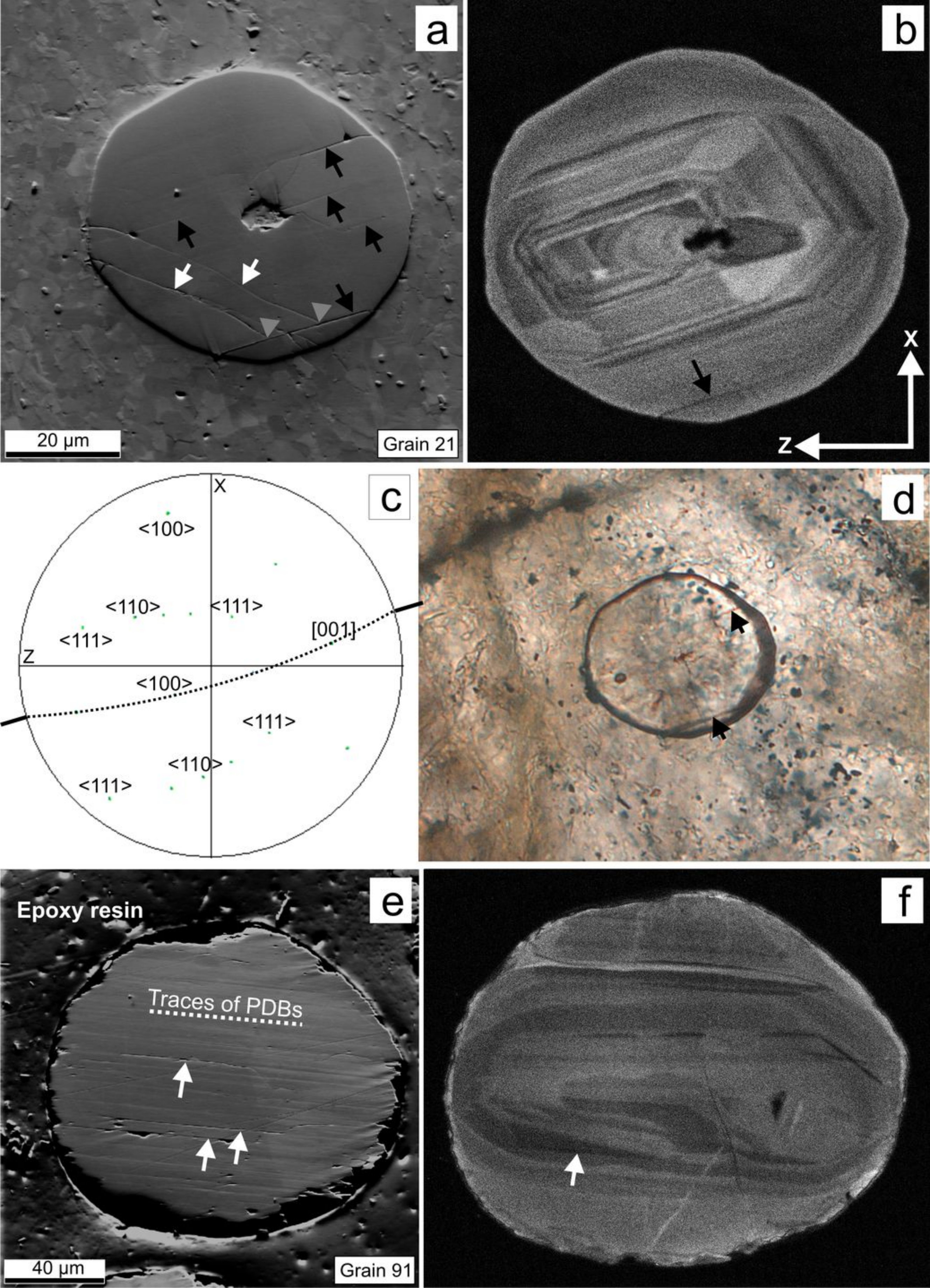
a
20 µm
Grain 21
b
x
z
c
X
Z
<100>
<110>
<111>
<111>
[001]
<100>
<111>
<110>
<111>
d
e
Epoxy resin
Traces of PDBs
40 µm
Grain 91
f

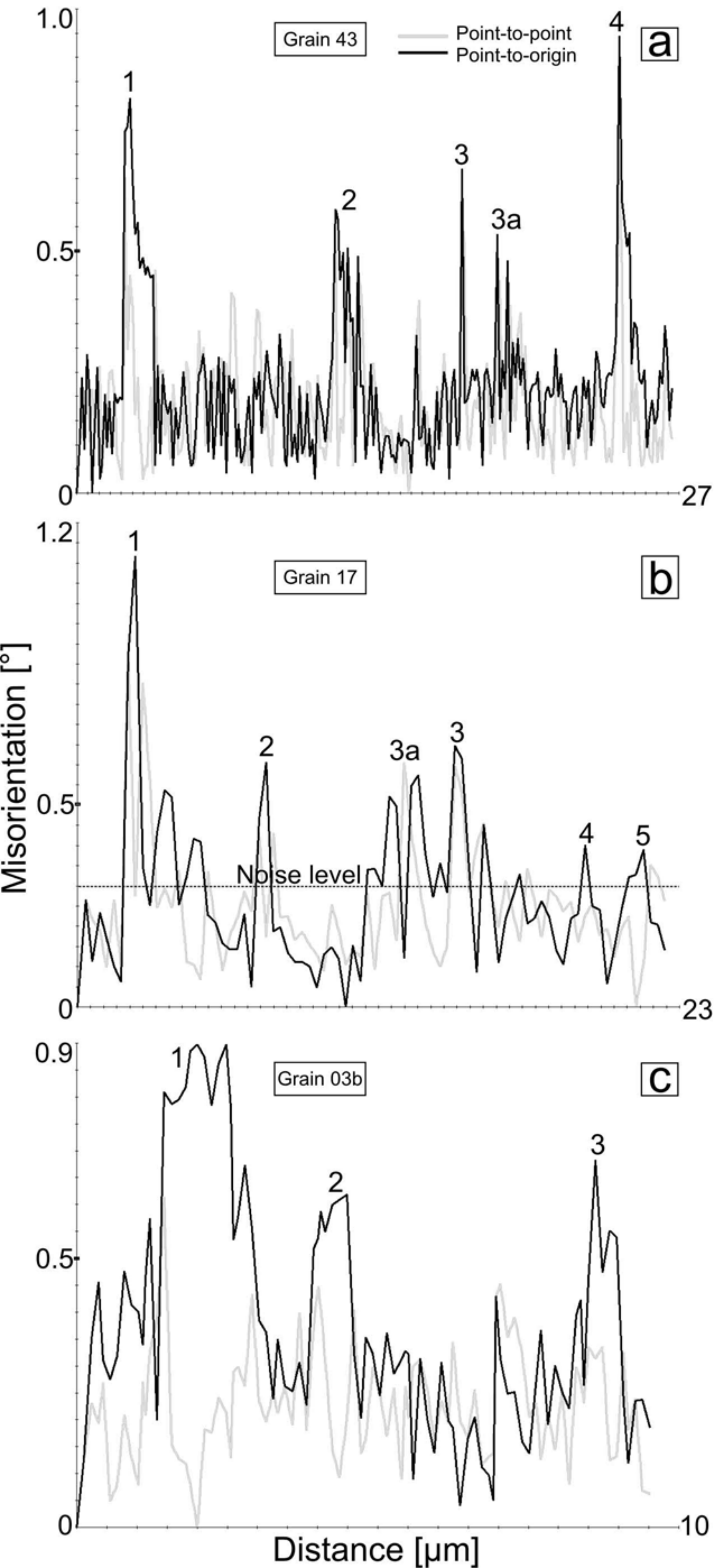
a
Grain 43
Point-to-point
Point-to-origin
1.0
0.5
0
27
1
2
3
3a
4
b
Grain 17
1.2
0.5
0
23
Noise level
1
2
3a
3
4
5
c
Grain 03b
0.9
0.5
0
10
1
2
3
Misorientation [°]
Distance [µm]

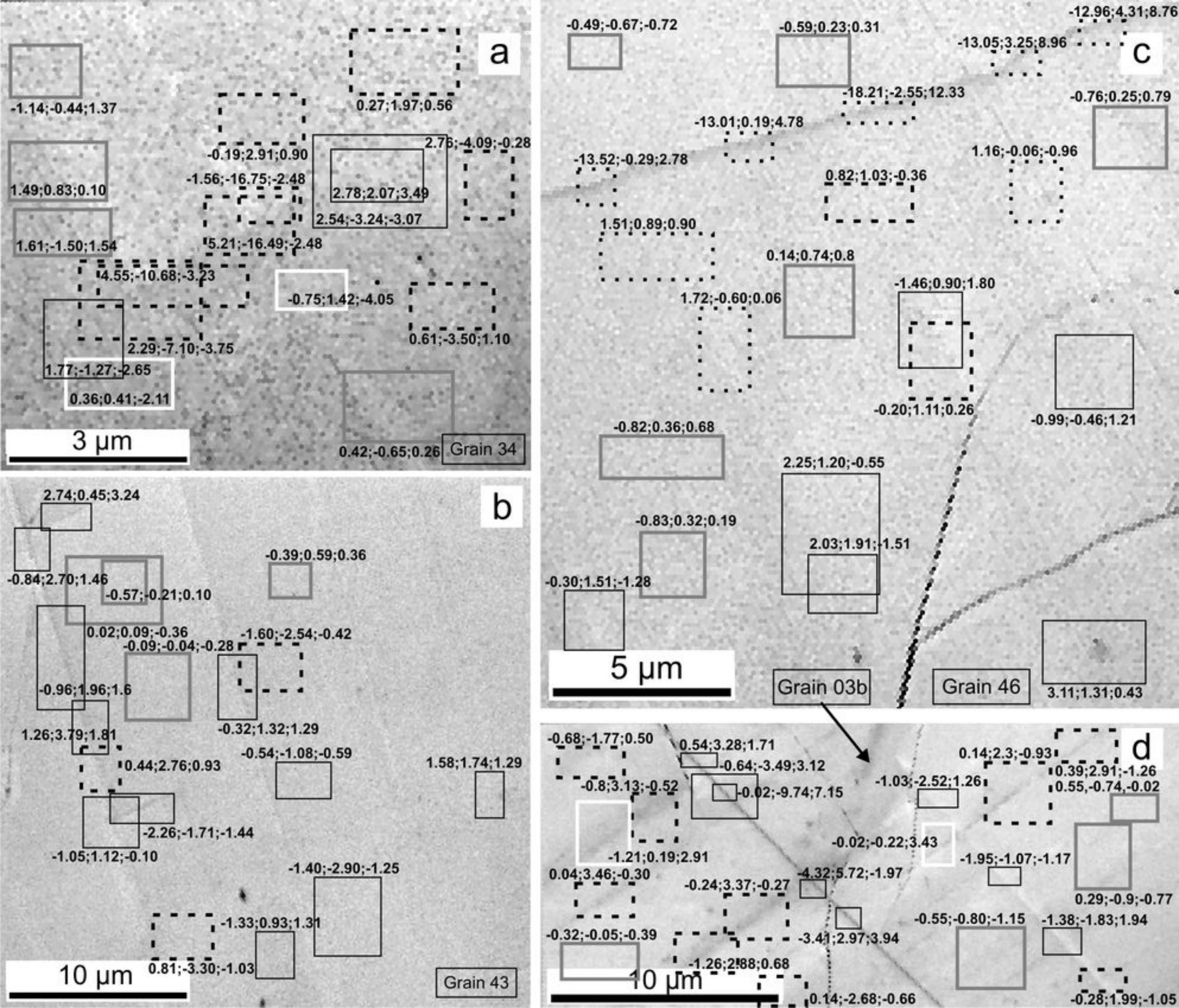
a
-1.14;-0.44;1.37
0.27;1.97;0.56
-0.19;2.91;0.90
2.76;-4.09;-0.28
1.49;0.83;0.10
-1.56;-16.75;-2.48
2.78;2.07;3.49
2.54;-3.24;-3.07
1.61;-1.50;1.54
5.21;-16.49;-2.48
4.55;-10.68;-3.23
-0.75;1.42;-4.05
2.29;-7.10;-3.75
0.61;-3.50;1.10
1.77;-1.27;-2.65
0.36;0.41;-2.11
3 µm
0.42;-0.65;0.26
Grain 34
b
2.74;0.45;3.24
-0.39;0.59;0.36
-0.84;2.70;1.46
-0.57;-0.21;0.10
0.02;0.09;-0.36
-1.60;-2.54;-0.42
-0.09;-0.04;-0.28
-0.96;1.96;1.6
-0.32;1.32;1.29
1.26;3.79;1.81
-0.54;-1.08;-0.59
0.44;2.76;0.93
1.58;1.74;1.29
-2.26;-1.71;-1.44
-1.05;1.12;-0.10
-1.40;-2.90;-1.25
-1.33;0.93;1.31
0.81;-3.30;-1.03
10 µm
Grain 43
-0.49;-0.67;-0.72
-0.59;0.23;0.31
-12.96;4.31;8.76
-13.05;3.25;8.96
c
-18.21;-2.55;12.33
-0.76;0.25;0.79
-13.01;0.19;4.78
1.16;-0.06;-0.96
-13.52;-0.29;2.78
0.82;1.03;-0.36
1.51;0.89;0.90
0.14;0.74;0.8
-1.46;0.90;1.80
1.72;-0.60;0.06
-0.20;1.11;0.26
-0.99;-0.46;1.21
-0.82;0.36;0.68
2.25;1.20;-0.55
-0.83;0.32;0.19
2.03;1.91;-1.51
-0.30;1.51;-1.28
5 µm
Grain 03b
Grain 46
3.11;1.31;0.43
-0.68;-1.77;0.50
0.54;3.28;1.71
-0.64;-3.49;3.12
0.14;2.3;-0.93
d
0.39;2.91;-1.26
-0.8;3.13;-0.52
-0.02;-9.74;7.15
-1.03;-2.52;1.26
0.55,-0.74,-0.02
-0.02;-0.22;3.43
-1.21;0.19;2.91
-1.95;-1.07;-1.17
0.04;3.46;-0.30
-4.32;5.72;-1.97
-0.24;3.37;-0.27
0.29;-0.9;-0.77
-0.55;-0.80;-1.15
-1.38;-1.83;1.94
-0.32;-0.05;-0.39
-3.41;2.97;3.94
-1.26;2.88;0.68
10 µm
0.14;-2.68;-0.66
-0.28;1.99;-1.05

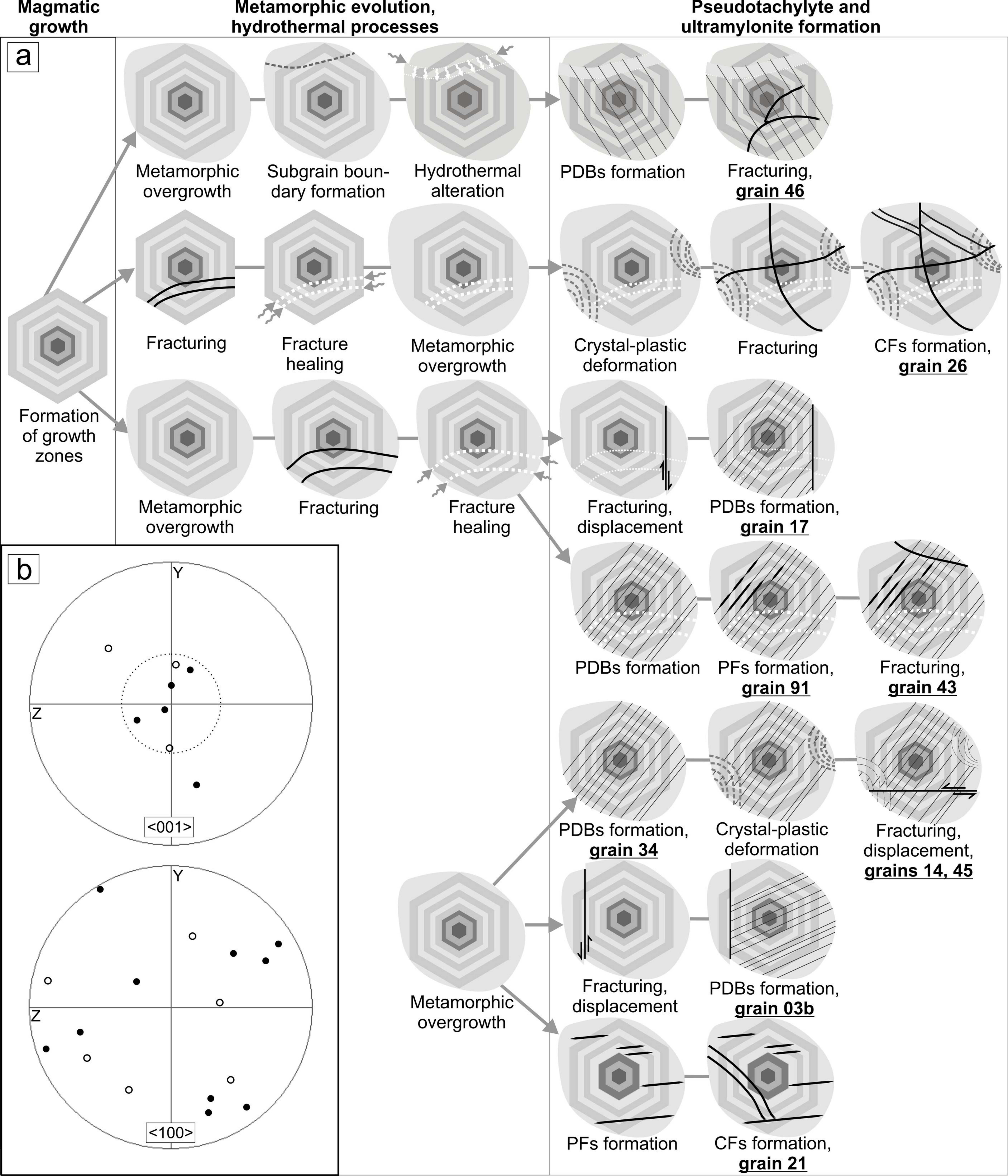
Magmatic growth
Metamorphic evolution, hydrothermal processes
Pseudotachylyte and ultramylonite formation
a
Metamorphic overgrowth
Subgrain boundary formation
Hydrothermal alteration
PDBs formation
Fracturing, **grain 46**
Fracturing
Fracture healing
Metamorphic overgrowth
Crystal-plastic deformation
Fracturing
CFs formation, **grain 26**
Formation of growth zones
Metamorphic overgrowth
Fracturing
Fracture healing
Fracturing, displacement
PDBs formation, **grain 17**
PDBs formation
PFs formation, **grain 91**
Fracturing, **grain 43**
PDBs formation, **grain 34**
Crystal-plastic deformation
Fracturing, displacement, **grains 14, 45**
Metamorphic overgrowth
Fracturing, displacement
PDBs formation, **grain 03b**
PFs formation
CFs formation, **grain 21**
b
Y
Z
<001>
Y
Z
<100>